

# Interpreting the Spectro-Temporal Properties of the Black Hole Candidate Swift J151857.0-572147 during its First Outburst in 2024

KAUSHIK CHATTERJEE,<sup>1</sup> S. PUJITHA SURIBHATLA,<sup>2</sup> SANTANU MONDAL,<sup>2</sup> AND CHANDRA B. SINGH<sup>1</sup>

<sup>1</sup>South-Western Institute For Astronomy Research, Yunnan University, University Town, Chenggong, Kunming 650500, China

<sup>2</sup>Indian Institute of Astrophysics, II Block, Koramangala, Bengaluru 560034, Karnataka, India

## ABSTRACT

For the first time, in March 2024, the transient Galactic black hole candidate Swift J151857.0-572147 experienced an outburst. Using publicly available archived *Insight*-HXMT data, we analyze the timing and spectral features of this source. Through model fitting of the power density spectrum, we were able to extract the properties of quasi-periodic oscillations, and based on those properties, we have determined that the QPOs are of type C. We also conclude that the shock instabilities in the transonic advective accretion processes surrounding black holes may be the source of the QPOs. This shock instability could produce variabilities of flux up to 48 keV, as we checked from the QPO energy dependence. High-frequency QPO is not observed during this period. In the broad energy band of 2 – 100 keV, simultaneous data from the three on-board instruments of *Insight*-HXMT were used to perform the spectral analysis. A combination of models, including broken power-law, multi-color disk-blackbody continuum, interstellar absorption, and reflection in both neutral and ionized medium were needed for spectral fitting to obtain the best fit. We discovered that at the beginning of the analysis period, the source was in an intermediate state and was transitioning toward the softer states based on the spectral features. It has a hydrogen column density of  $(4.3 - 6.9) \times 10^{22} \text{ cm}^{-2}$ .

**Keywords:** X-rays: binary stars; black holes; Stellar accretion disks; Shocks; Compact radiation sources

## 1. INTRODUCTION

X-ray binaries (XRBs) are quite common and important astronomical binary systems. Since accretion serves as the power source in these systems, it is crucial to understand them (Frank, King & Raine 2002). The primary object in XRBs is a compact object, and the secondary object is a companion star. The compact object may be a neutron star or a black hole, which are both the remnants of stellar bodies. There are multiple categories for XRBs. They fall into two main categories based on the companion's mass: low-mass X-ray binaries (LMXRBs) and high-mass X-ray binaries (HMXRBs) (Remillard & McClintock 2006). Transient and persistent sources are the other categories into which XRBs are divided, based on the type of variability in their outbursts. While transient sources occasionally exceed detection levels and primarily remain in quiescence, or the dormant state ( $L < 10^{32} \text{ erg/s}$ ; Hannikainen et al. 2005), flux or counts of persistent sources remain higher than just the detection level most of the time ( $L > 10^{36} \text{ erg/s}$ ; Chen et al. 1997). These transients experience outbursts that can endure for several weeks or even months (Tetarenko et al. 2016).

Though the population of transient HMXBs is increasing, the majority of reported transients are LMXBs (McClintock et al. 2013; Remillard & McClintock 2006 for a review as well). As per Debnath et al. (2010), there are two main categories of BH outbursts based on their nature: slow rise slow decay (SRSD) and fast rise slow decay (FRSD). Zhang et al. (2019) divided outbursts into many types, such as glitter, reflare, multipeak, mini-outburst, or new-outburst, based on their rebrightening characteristics.

The soft multi-color thermal black body and the hard non-thermal power-law components combine to form the spectrum of a black hole. The hard component can be explained by physical scenario in the Comptonizing region, also referred to as the 'Compton Cloud', which is the repository of hot electrons (Sunyaev & Titarchuk 1980, 1985). The soft component is modeled as the radiation of the standard Keplerian disk (Shakura & Sunyaev 1973, hereafter SS73). Over time, numerous models have been proposed to describe the hard component of the composite spectrum of a stellar-mass black hole, e.g., the thick disk model (Paczynski & Witta 1980). Even though they did a good job of explaining it, they all made some very specific assumptions. In 1995, Chakrabarti and his collaborators developed the two-component advective flow (TCAF, Chakrabarti & Titarchuk 1995) system, which provided a more comprehensive solution.

A transient black hole experiences many phases and spectral types during an outburst (Remillard & McClintock 2006). Generally speaking, during an outburst, we wit-

Corresponding author: Kaushik Chatterjee

kaushik@ynu.edu.cn, mails.kc.physics@gmail.com

santanuicsp@gmail.com

chandrasingh@ynu.edu.cn

ness four distinct BH spectral states, which are hard state (HS), hard intermediate state (HIMS), soft intermediate state (SIMS), and soft state (SS), respectively. An outburst usually starts in the HS. After that, it moves to the HIMS and the SIMS as brightness increases. At last, when the source's brightness peaks, it shifts to the SS. This is referred to as the outburst's rising phase. The source then transits back to the HS in the opposite cycle as the brightness gradually drops to its minimum. This is referred to as the outburst's declining phase. To put it briefly, a BH's spectral state transition forms a hysteresis loop in the order listed below: HS (rising)  $\rightarrow$  HIMS (rising)  $\rightarrow$  SIMS (rising)  $\rightarrow$  SS  $\rightarrow$  SIMS (declining)  $\rightarrow$  HIMS (declining)  $\rightarrow$  HS (declining). A source that experiences all four of the aforementioned often observed spectral states during some outbursts is known as type-I outbursts. In type-II or failed outburst, the source does not go to soft state (Tetarenko et al. 2016).

Understanding temporal aspects is just as critical to comprehending the dynamics of the accreting flow around the BHs as rich spectrum features and variabilities. It has been noted that the light curves exhibit extremely tiny timescale variabilities during an outburst, particularly in the high-energy bands. Variabilities like broadband noise and narrow characteristics in the power density spectrum, or PDS, are imprinted by the Fourier transformation of the light curve (van der Klis 1989). A power-law function is used to describe the broadband noise, which is dispersed over a wide frequency range. Lorentzian profiles can be used to describe the quasi-periodic oscillation (QPO), which is a power peak in restricted frequency ranges. Because of their geometrical origin, low-frequency QPOs (LFQPOs) are frequently detected in BHXRBs. Types A, B, and C are the three categories into which LFQPOs are divided, based on characteristics such as frequency ( $\nu$ ),  $Q$ -value ( $= \nu/\delta\nu$ , where  $\delta\nu$  is the full width at half maximum, or FWHM), (%) RMS, etc. (Casella et al. 2005). High-frequency QPOs can also be seen in BHXRBs, although it is quite rare. Shock oscillation model (Molteni et al. 1996; Chakrabarti et al. 2005, 2008, 2015), magneto-acoustic waves (Titarchuk et al. 1998), accretion-ejection instability (Tagger & Pellat 1999), Lense-Thirring precession (Stella et al. 1999; Ingram et al. 2009), and other theories have been proposed, though their origin is still up for debate. Shock oscillation model seems to be a more complete one since it can simultaneously describe the temporal and spectral features.

It is thought that spectral and timing properties are related since they originate from the same system and because variations in spectral states can also affect the kinds of QPOs. When examining the two solely in terms of the features of the light curve, such as the hardness ratio, or HR, and the hardness intensity diagram, or HID, a strong association is seen (Homan et al. 2001). Accretion rate ratio intensity diagrams, or ARRIDs, can be used to understand how variations in viscosity or different mass accretion rates interact, as some model-fitted approaches also demonstrated (Chatterjee et al. 2020). Links between spectral and temporal features from pure observational ground can also be established using the

RMS-intensity diagram, or RID (Munoz-Darias et al., 2011), and the hardness ratio-intensity diagram, or HRD (Belloni et al., 2005).

First identified by Swift/XRT as a GRB (GRB 20240303A; Kennea et al. 2024), the new Galactic transient Swift J151857.0-572147 was found in Swift Trigger 1218452 (GCN 35849). But thereafter, it was determined to be a Galactic transient due to its constant brightness and location in the Galactic plane. The RA and Dec of the source were determined to be RA(J2000) = 15h18m57.00s and Dec(J2000) =  $-57^{\circ}21'47.9''$  based on the optimal source localization utilizing XRT instantaneous on-board localization (Kennea et al. 2024). On March 4, 2024, during 15 minutes, from 02:13:13.3 to 02:28:08.9 (MJD 60373.1), follow-up radio observations were conducted using the MeerKAT telescope at 1.28GHz (L-band) with a bandwidth of 856 MHz at flux density of 10 mJy (Carotenuto et al., 2024; Cowie et al., 2024). The source's nature was identified as consistent with an X-ray binary in the hard state by using the inverted radio spectrum ( $f(\nu) \propto \nu^\alpha$ , where  $\nu \sim +0.5$ ) in conjunction with the photon index. This suggested that the source might be a black hole or a neutron star. On March 9, 2024, from UT 10:35:10 to UT 11:06:20 (MJD 60378.45), the Australia Telescope Compact Array (ATCA) simultaneously recorded radio observations at frequencies of 5.5 and 9 GHz (Saikia et al., 2024). Additionally, their investigation confirmed the source to be a Galactic black hole. Target of opportunity (ToO) was carried out on this source with an exposure of 1000s by Swift/XRT following the ATCA. According to Del Santo et al. (2024), it was discovered that the combination of the phenomenological disk black body (diskbb) and power-law (po) model models describes the spectrum quite well. These discoveries also confirmed that the source is a black hole. The source was detected by INTEGRAL serendipitously on March 8, 9, 10, and 11 of 2024 (Sguera 2024). The 60cm Robotic Eye Mount (REM) telescope observed the source in both optical and near-infrared wavelengths as part of the monitoring program of GRBs (Baglio et al. 2024). Optical measurements of the source were also carried out by the Las Cumbres Observatory (LCO) network (Saikia et al. 2024).

From their Swift/XRT spectral modeling, Kennea et al. (2024) found a column density of  $N_H = 5.6 \pm 0.06 \times 10^{22} \text{ cm}^{-2}$ . Additionally, they observed a power-law photon index of  $\Gamma = 1.78 \pm 0.02$ . While Burridge et al. (2024) reported that the source's distance was  $4.48_{-0.47}^{+0.67}$  kpc, with an HI absorption towards it, the absence of positive velocity absorption lines towards other sources in the field of the HI absorption for this source puts an upper limit on the distance as  $15.64_{-0.60}^{+0.77}$  kpc. The mass and spin parameters of the source are reported to be  $\sim 9.2 \pm 1.6 - 10.5 \pm 1.8 M_\odot$  and  $\sim 0.65$ , while the possible inclination is  $\sim 38^\circ \pm 8^\circ - 47^\circ \pm 15^\circ$  and 0.65 (Mondal et al. 2024).

## 2. OBSERVATION AND DATA REDUCTION AND ANALYSIS

This source has recently been observed by Swift satellite. It is currently being monitored at the time of this manuscript writing by various other X-ray satellites, e.g., NICER, NuSTAR, IXPE, etc. We use X-ray data from China’s first X-ray mission *Insight-HXMT* (Zhang et al. 2020). After the onset of the outburst, 7 observation IDs were available publicly when we started our analysis. We list the data in Table 1 below.

Each of these observation IDs has multiple exposures (up to 14 for some). While listing our analysis results, we will list all those exposure IDs with MJD. Using raw data from all these obs IDs, we first produced science-analyzable, cleaned data and then performed our analysis. We discuss data reduction and analysis in the following subsections.

### 2.1. Data Reduction

Following the on-demand retrieval of level-1 data from the repository, we generated cleaned level-2 data for scientific study. The raw data cleaning procedure was carried out as follows. With the *HXMTDAS*<sup>1</sup> (version 2.05) software, we execute the `hpipeline` command using appropriate input and output directories. For each of the three instruments, this pipeline executes a series of automatic commands. However, there are a few prerequisites that must be met. Specific parameters were established to achieve good time interval (GTI), such as elevation angle  $> 10^\circ$ , geomagnetic cutoff rigidity  $> 8 GV$ , pointing offset angle  $< 0.04^\circ$ , and distance from the South Atlantic Anomaly (SAA)  $> 600$  s. To facilitate background analyses, each telescope carries large and small field-of-view (FOV) detectors. The small FOV detectors are more suitable for pointing observation as they have a lower probability of source contamination<sup>2</sup>. Together, these commands extract, clean, and produce science products that are ready for analysis. The *HXMT Manual*<sup>3</sup> contains a detailed discussion on this. The spectra for the HE, ME, and LE instruments are generated using the particular commands `hespecgen`, `mespecgen`, and `lespecgen`. On the other hand, the light curve files for the three instruments are created using the commands `helcgen`, `melcgen`, and `lelcgen`. Appropriate response files are generated by `herspgen`, `merspgen`, and `lerspgen`. The commands `hebkmap`, `mebkmap`, and `lebkmap` for instruments HE, ME, and LE, respectively, were used to do the background subtraction for both the timing and spectral data. We group the spectrum using the `grppha` task of *FTOOLS* to a minimum of 30 counts per bin for  $\chi^2$  fit-statistics in *XSPEC*. Additionally, to generate appropriate light curves for PDS generation and QPO search, we adjusted the time bin size to 0.01 s. To search for high-frequency QPOs (HFQPOs), we also produced 1 ms time-binned light curves for all the available exposures. The HE light curve covers a broad range of 27 – 250 keV. To check the energy dependence of QPOs, we

**Table 1.** List of Data used. Column 1 lists each observation ID. In columns 2 and 3, we give the start and end date and time of each observation ID. Column 4 gives the exposure time of each observation ID.

Obs. Id. <sup>[1]</sup>	Start UT <sup>[2]</sup>	End UT <sup>[2]</sup>	Exp. (s) <sup>[3]</sup>
(1)	(2)	(3)	(4)
P0614374001	2024-03-04 20:08:55	2024-03-06 02:13:33	108278
P0614374002	2024-03-06 02:13:31	2024-03-08 01:43:18	170987
P0614374003	2024-03-08 01:43:22	2024-03-10 02:48:37	176715
P0614374004	2024-03-10 02:48:37	2024-03-12 00:47:47	165550
P0614374005	2024-03-12 10:14:15	2024-03-12 19:53:12	34737
P0614374006	2024-03-13 09:59:33	2024-03-15 09:32:39	171186
P0614374008	2024-03-17 12:09:52	2024-03-17 21:39:51	34199

produced 0.01 s time-binned HE light curves in seven different energy bands (27 – 35, 35 – 48, 48 – 67, 67 – 100, 100 – 150, 150 – 200, 200 – 250 keV). Along with this, we also cut light curves in the 48 – 250 keV energy band for all the HE exposures. The reason for this will be discussed in later sections.

Detailed analysis using these cleaned light curves and spectra files is discussed in the next subsection.

### 2.2. Data Analysis

We conduct spectral and temporal research on the black hole candidate (BHC) Swift J151857.0-572147’s very first outburst in 2024. First, we created 0.01 s time-binned light curves using data from the LE, ME, and HE modules of the HXMT. The fast Fourier transformation (FFT) in the `powspec` task of the *XRONOS* package in the *HEASoft* software was used to construct the power density spectrum (PDS) based on those light curves. The data from each observation was split up into many intervals, with 8192 new bins in each interval. To create the final PDS, the PDS for each interval must first be generated and then averaged. The PDS is normalized using the Leahy normalization (Leahy et al. 1983). A geometrical rebinning of -1.02 is applied. We used these procedures to look for LFQPOs. Utilizing a Lorentzian model in `powspec`, we fit the QPO shape and derive QPO properties such as frequency ( $\nu_{qpo}$ ), full-width at half maximum (FWHM) and normalization. We have detected the presence of harmonics in several observations. Additionally, we have derived their properties by Lorentzian model fitting. We fitted the light curves of all the exposures for three energy bands LE (2 – 10 keV), ME (10 – 35 keV), and HE (27 – 250 keV) of the listed (Table 1) 7 observations. We report them next in the result section.

We also studied the energy dependence of the PDS using only the HE light curves. As mentioned above, we extracted 0.01 s time-binned HE light curves into 7 different energy bands (mentioned in the data reduction section) as HE covers a large energy range. We searched for only those exposures in which LFQPO was present at the full energy band. Using those 7 light curves separately, we produced PDS in the same way as mentioned above. Using the same model approach, we extracted QPO information like  $\nu_{qpo}$ , FWHM, and nor-

<sup>1</sup> <http://hxmt.org/index.php/usersp/dataan>

<sup>2</sup> <http://hxmtcn.ihep.ac.cn/AboutHxmt.jhtml>

<sup>3</sup> <http://hxmtcn.ihep.ac.cn/SoftDoc/501.jhtml>

malization. We also did the same for the 48 – 250 keV HE light curve.

Using these fitting estimations ( $v_{qpo}$ , FWHM, norm), we also estimated some properties of the QPOs that help designate their nature. This will be discussed in the result section.

For HFQPOs, we followed the same procedure, except only using the 1 ms time-binned light curves for all the exposures for all three energy bands.

We also used all three modules (LE, ME, and HE) for spectral analysis, fitting the broadband data in the 2 – 150 keV energy range. First, we tried to do the spectral analysis using a combination of simple disk blackbody and power-law models. However, we did not find an acceptable fit. This is discussed later. The combinations of disk blackbody, broken power-law models yielded the best fit for the data, according to our search. We have employed the `tbabs` model for interstellar absorption. Since we are simultaneously fitting all three modules, we have included a constant to normalize the three resultant fittings. The following is our best model fit combination: `constant*tbabs*(diskbb + broken power-law)`. We take this as our Model-1. We also tried to analyze spectral data using reflection model `pexrav`. For that, our model combination reads as: `constant*tbabs*(diskbb + pexrav)`. We take this as our Model-2. We also tried to use the reflection model `pexriv` which accounts for ionized medium. Thus, `constant*tbabs*(diskbb + pexriv)` reads as our Model-3. Systematic errors were added to perform spectral analysis, as suggested in the HXMT manual. Not every exposure ID of the specified observation IDs was subjected to spectral analysis. We did not spectrally analyze every exposure, compared to the time analysis. Table 2 indicates the spectrally analyzed exposures with a ‘\*’. This is because: in the case of timing analysis, we observed variations in timing properties in a single day, but in the case of spectrum analysis, the properties do not significantly change over a short period. We include them in the section on results. We also tried to spectrally fit the exposures using a relativistic reflection model `relxill` (Dausar et al. 2016). However, we did not find an acceptable fit for all the observations. This will be discussed later.

### 3. RESULTS

We discuss our results from the timing and spectral analysis in the following subsections. However, before going into the analysis results, we discuss the variation of the flux of the source during the outburst first below.

#### 3.1. Timing Properties

First, we will discuss the outburst evolution from the light curve profiles and hardness ratio, and then we will discuss our analysis of QPOs.

##### 3.1.1. Outburst Profile, and Hardness Ratio

The BHC Swift J151857.0-572147 was not observed by the MAXI/GSC instrument. The source is located at  $\sim 0.2^\circ$

from the source Cir X-1. Although the facility could identify the brightening of the source, the two sources could not be resolved separately. In Figure 1, we show the location of the two sources in the upper panel. It can be noticed that the two sources are located very close to each other. The lower panel of the figure shows increased activity due to the outburst of Swift J151857.0-572147.

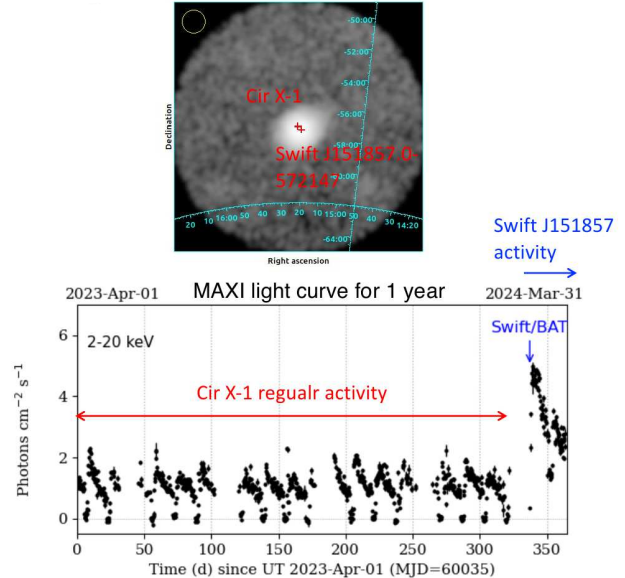


**Figure 1.** MAXI/GSC field of view and source activity for the sources Cir X-1 and Swift J151857.0-572147 (Credits: MAXI Team).

In Figure 2, we show the variation of the count rates for around 15 days. The count rates are extracted using LE, ME, and HE light curves of HXMT in the 2 – 10, 10 – 35, and 27 – 250 keV energy bands. In panel (a), we show the variation of those source and background count rates for the three bands (in respective colors). Red is for LE, while green and blue colors are used to represent ME and HE bands. The filled circle (of each color) lines represent the source counts, whereas the triangle-shaped lines represent the background count rates. As can be noticed, the HE background count rate was quite high and was almost comparable to the source count rate. The other two bands showed a significant difference in count levels between source and background. In Table 2, we list the start, end, and average MJDs of all our analyzed exposures. We also list the source and background count rates for LE, ME, and HE in Table 2. In panel (b) of Figure 2, we show the count rates in 2 – 4, 4 – 10 keV energy bands, which are extracted using LE light curves. In panel (c), the hardness ratio (HR) is plotted using the ratio of the LE count rates of 4 – 10 to 2 – 4 keV.

From the light curves, we see that the source is quite bright during the outburst. The LE count rate shows a smoother variation than the ME and HE bands, which can also be noticed in the (b) panel. From the variation, HR gives a rough idea that the source had already moved past its hard state

## Evolution of LC, and HR

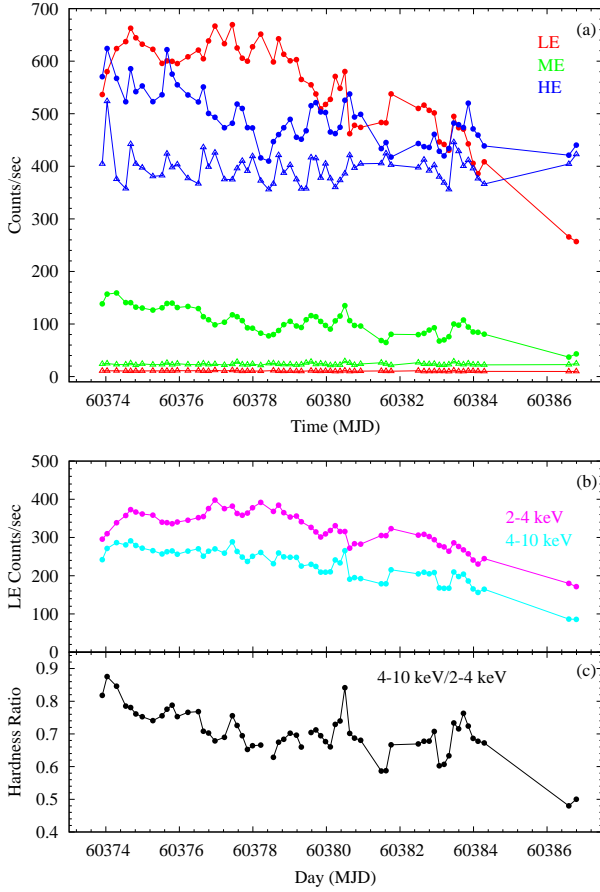


**Figure 2.** Variation of *Insight*-HXMT (a) source and background count rates in LE, ME, and HE bands, (b) 2 – 4 keV and 4–10 keV LE count rates, (c) hardness ratio (HR; 4 – 10 keV/2 – 4 keV) with time.

as *Insight*-HXMT started monitoring the source. As time progressed, spectral nature progressed from intermediate to softer states. However, we need timing and spectral analysis results to designate this firmly. We discuss them in the next two subsections.

### 3.1.2. Low-Frequency Quasi Periodic Oscillations

We created the PDS to analyze QPOs using the 0.01 sec time-binned light curves from all three bands (LE, ME, and HE), as stated in §2. In Figure 3, we show the best model-fitted PDS continuum for the three bands (a) LE, (b) ME, and (c) HE for the observation ID P0614374001 (exposure ID: P061437400101-20240304-01-01). While, both the QPO and harmonic were present in the LE band, the harmonic nature was absent in ME and was not very prominent in HE. The QPO and harmonic have a 1:2 ratio in frequency with the  $\nu_{\text{harmonic}} \sim 6.43 \pm 0.04$  Hz. The harmonic in this exposure has an FWHM of  $0.39 \pm 0.13$  and normalization of  $0.57 \pm 0.14$ . We discover that each of the three energy bands' light curves has a fundamental QPO nature. We first checked all the expo-

## Model fitted PDS continuum

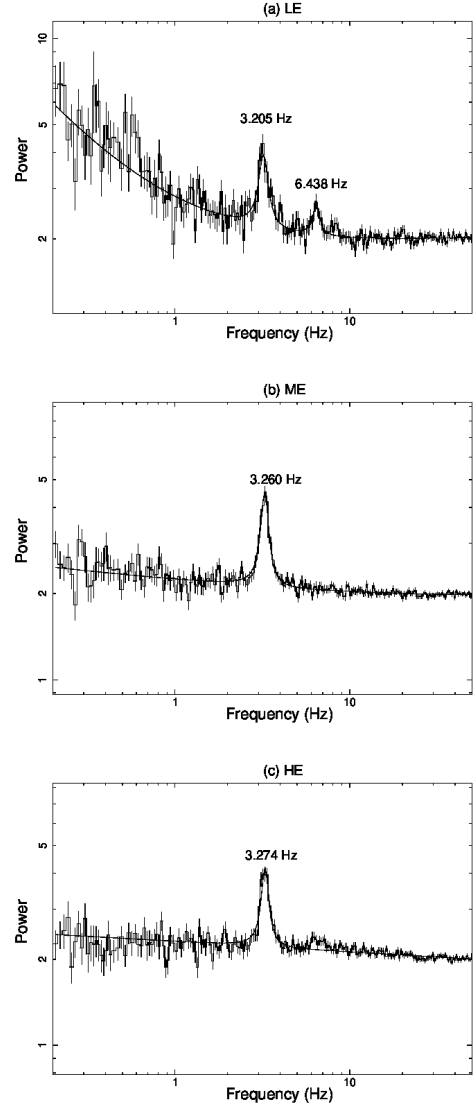


**Figure 3.** Model fitted power density spectrum (PDS) continuum in 0.2 – 50 Hz for (a) LE, (b) ME, and (c) HE. The best fit is achieved using a combination of a set of models: *power-law*, *linear*, *constant*, and *Lorentzian*.

sure for the observation ID P0614374001. From our fitting, we first extracted the basic QPO information, which are QPO frequency ( $\nu_{qpo}$ ), full-width at half-maximum (FWHM or LW), and QPO normalization (LN).

We found that QPO was present in most of the exposures of this observation ID. It was present for all exposures in the ME band and was absent in the last LE band and second and fifth HE band. Also, the QPO frequency evolved within the short period of the duration of this observation ID. Thus, we checked for QPOs for all the exposures. At the start of our analysis period, fundamental QPO was present in almost most of the exposures. The  $\nu_{qpo}$  was  $\sim 3.2$  for all three bands

on MJD 60373.9, and it increased as the outburst progressed. Then after some days, it decreased, and then again showed an increasing trend. Then, it again decreased and increased and decreased and continued this way. The highest frequency in the LE band was 8.1 Hz on MJD 60376.9, on which both the light curves in the ME and HE bands were not created by the `hpipeline` command. The highest frequency in the ME band was 8.97 Hz on MJD 60377.9, on which the LE and ME light curves were not produced. In the HE band,  $\nu_{qpo}$  was the highest on MJD 60379.3 with a value of 6.82 Hz. We show the variations of the QPO frequency during our full analysis period in Figure 4(a-c) for (a) LE, (b) ME, and (c) HE. In Table 3, we listed the values of  $\nu_{qpo}$  in columns 2, 3, & 4 for LE, ME, and HE. Although for the exposure P061437400103-20240305-02-01, there was a presence of a harmonic nature in the HE band, we did not fit it as the noise was high and the harmonic was like a broad Lorentzian feature. We did not find harmonic for any other exposures of any other observation ID in any of the three bands.

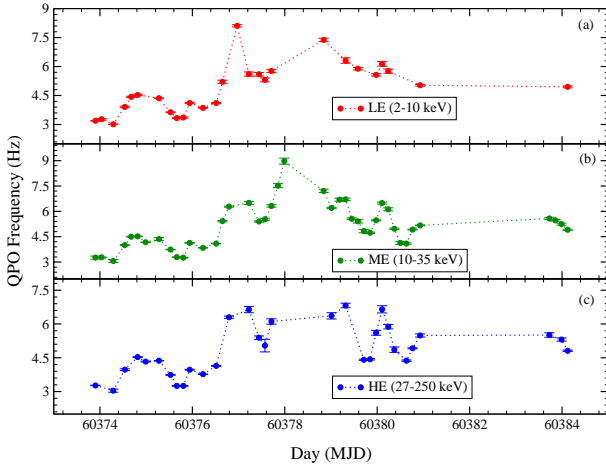


**Figure 4.** Evolution of QPO frequency with time during the whole period of analysis for (a) LE, (b) ME, and (c) HE.

We were able to extract certain information about QPOs, such as full-width at half maximum (FWHM) and Normalization (LN) by the use of PDS fitting. For the exposures, we additionally retrieved the source and background count rates. Using the formula from Bu et al. (2015), we estimated the fractional RMS as  $RMS = \sqrt{\frac{P}{S+B} \frac{S+B}{S}}$ , which denotes the fractional variability in the PDS. Here,  $S$ , and  $B$  represent the count rates of the source and the background, respectively.  $P$  is the Leahy normalized power. We also estimated the  $Q$ -factor ( $\nu/\delta\nu$ ), which measures the sharpness of the QPO. Table 3 lists these values for LE, ME, and HE in columns 5–7 ( $Q$ -value) and 8–10 (RMS), respectively. This is shown in Figure 5. The variations of the  $Q$  factor were consistent in the three different bands. To check if there is any correlation between the QPO RMS and QPO frequency, we plotted those two properties against each other in Figure 6. We have

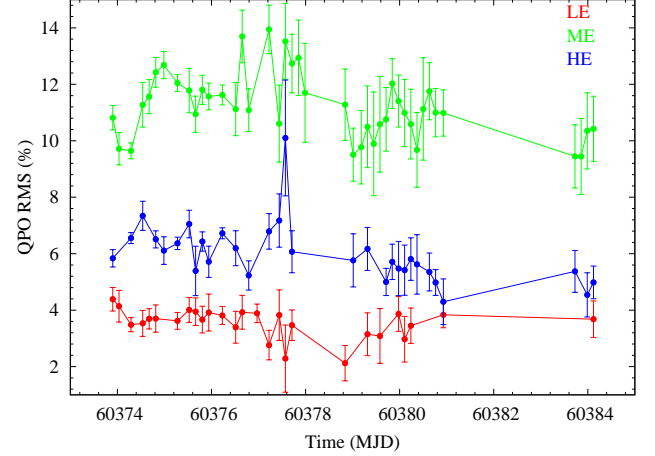


**Figure 5.** Variation of QPO RMS with time for the LE (red), ME (green), and HE (blue) bands, respectively.

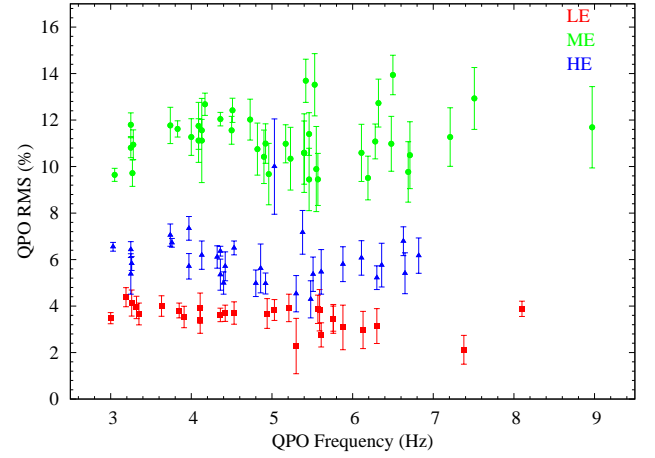


**Figure 6.** Variation of QPO RMS with QPO frequency for the LE (red), ME (green), and HE (blue) bands, respectively.

not found any correlation between them for this source in all three energy bands.

As explained before, we also checked the energy dependence of QPOs using the HE light curve in 7 different energy bands. These energy ranges were chosen to maintain similarity with Ma et al. (2023). The PDS continuums for the observation ID P0614374001 (exposure ID: P061437400101-20240304-01-01) are given in Figure 7(a-g) for respective energy bands. For this exposure, we find that the fundamental QPO was prominently present at 3.274 Hz in the 27 – 35 keV energy band, while it is also present in the 35 – 48 keV with a little change of frequency of 3.222 Hz. However, the nature of QPO was not as strong as in the 27 – 35 keV. Above 48 keV, we did not find any nature of fundamental QPO. We notice a sharp fall of QPO strength above 48 keV. Chatterjee et al. (2021) studied QPO energy dependence for the BHC GRS 1716-249 using AstroSat data. Although the fundamental QPO nature got weaker in high energies in that report, it

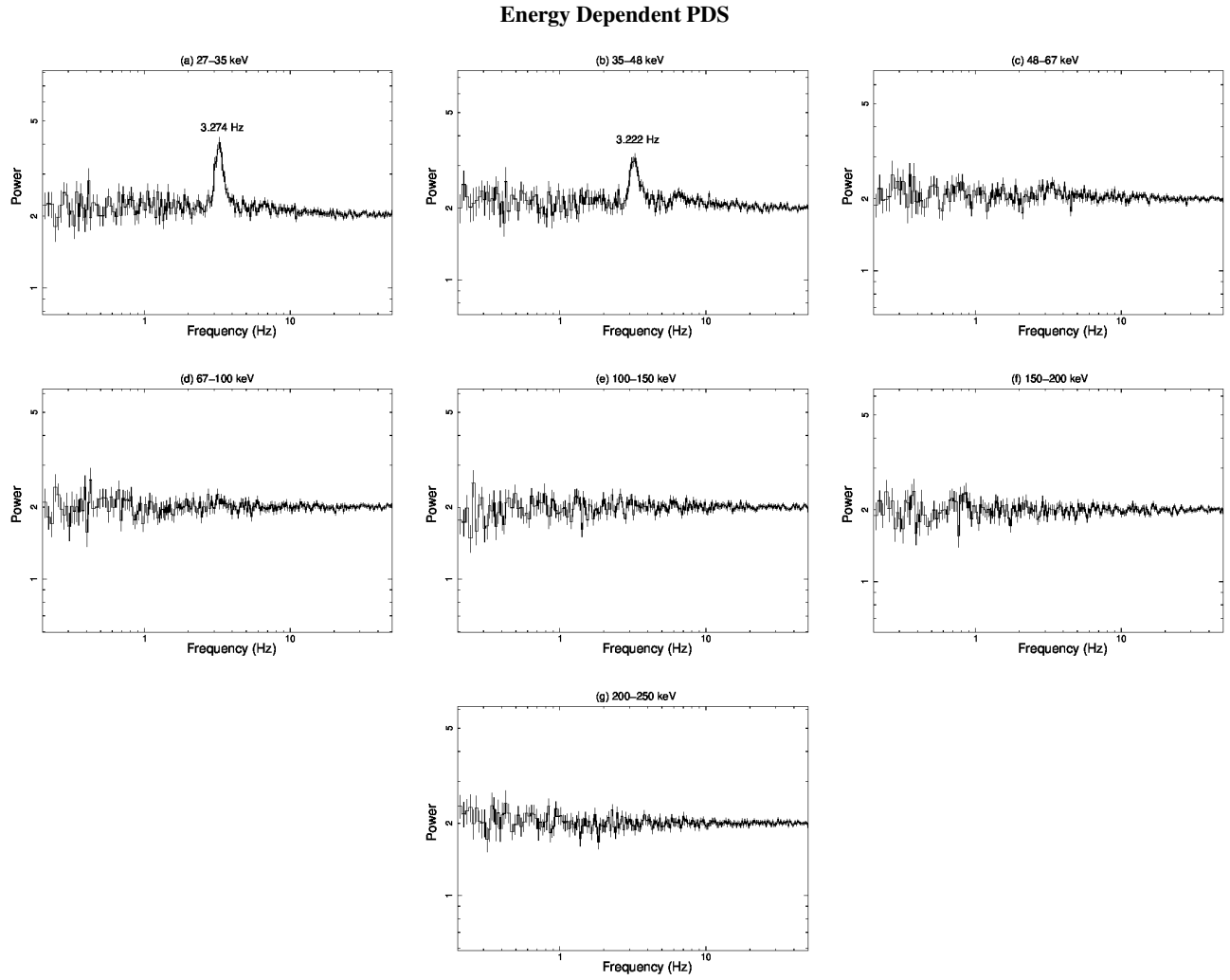


**Figure 7.** Energy dependent PDS, produced in (a) 27-35, (b) 35-48, (c) 48-67, (d) 67-100, (e) 100-150, (f) 150-200, and (g) 200-250 keV energy bands using 0.01 s time-binned HE light curves. This is for the observation ID P0614374001 (exposure ID: P061437400101-20240304-01-0).

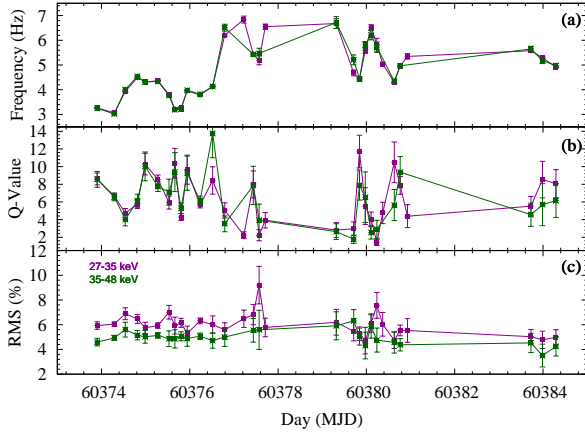


**Figure 8.** Variation of energy-dependent (a) QPO frequency (in Hz), (b) Q-factor, and (c) RMS (%) with time. Here, the magenta-colored points represent the values for 27–35 keV, whereas the green-colored points represent the values for 35–48 keV energy bands, respectively.

did not show this type of sharp fall of QPO nature after some energy band. A possible weak harmonic nature was noticed in the 35–48 keV band, which was not present in the 27–35 keV. However, it looks very weak and we did not model it. Harmonic nature was also not observed above 48 keV. We checked this for all the 31 exposures for which fundamental LFQPO was present in the HE light curve. We find that for all of these exposures, QPO was absent above 48 keV. For some exposures, we found that LFQPO was absent in the 35–48 keV band, although it was present in the 27–35 keV band.

Using the formulas, as mentioned above, we estimated  $Q$ -values and RMS (%) for all these exposures in both these bands. In Figure 8, we show the variation of QPO frequency,  $Q$ -value, and RMS (%) for all these exposures with time. We notice that the  $\nu_{qpo}$  varied in a very narrow range between these two energy bands, which is within the error range. The  $Q$ -value shows a random variation for both the bands, where it was sometimes higher for 27–35 keV bands and sometimes for 35–48 keV. The overall variation of RMS (%) was higher in case of 27–35 keV band, compared to the higher band. The values of the variation of QPO properties in case of energy dependence is given in the Table 4.

We also show the variation of QPO RMS with energy in Figure 9. We noticed that the QPO RMS was lowest in the LE band. It was the highest in the ME band. Then it started to decrease. Above 48 keV, we did not find the presence of any QPO.

Apart from this, we also searched for QPOs in the 48–250 keV energy band light curve. Since above 48 keV, no QPO was found, we wanted to check if the energy range was higher, it could show QPO nature or not. In all of the exposures, except one, we did not find the presence of QPO in this energy band. This is for the observation ID. P0614374001 (exposure ID. P061437400103-20240305-02-01). We found

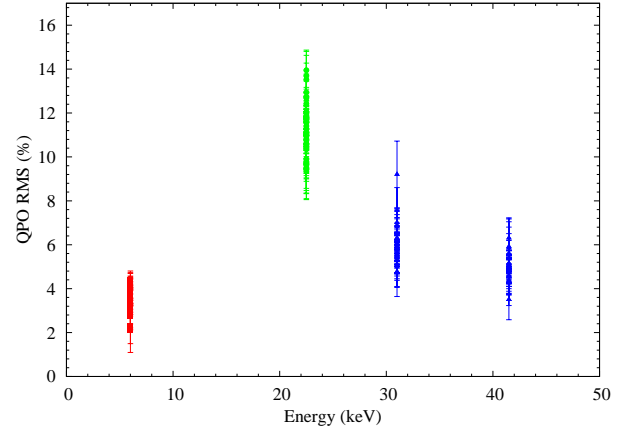


**Figure 9.** Variation of QPO RMS with energy. The red, green, and blue points represent data points using LE, ME, and HE bands light curves respectively for all the exposures.

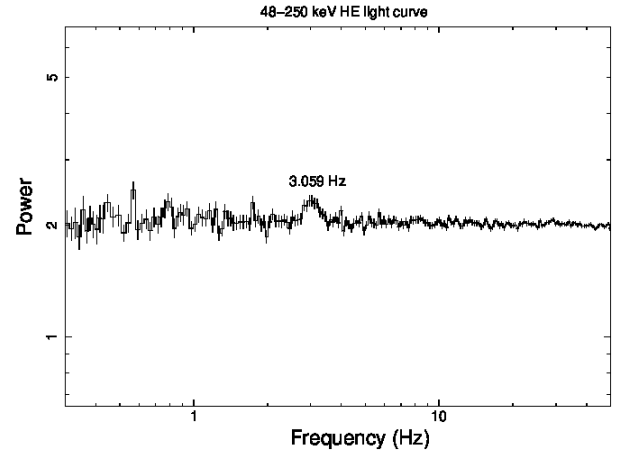


**Figure 10.** PDS in the 48–250 keV energy band for the HE light curve of the exposure ID. P061437400103-20240305-02-01

that there was the presence of a fundamental QPO in this exposure at  $3.06 \pm 0.05$  Hz. This is shown in the Figure 10.

### 3.1.3. High Frequency QPOs

Apart from looking for low-frequency QPOs, we also searched for high-frequency QPOs (HFQPOs) in all the light curves for the three bands in all 62 exposures. In Figure 11(a–c), we show the PDS continuum for 0.001 sec time-binned (Nyquist frequency = 500 Hz) curve for (a) LE, (b) ME, and (c) HE. However, we did not find any signature of HFQPOs in any of our light curves. The frequency in the PDS in LE, ME, and HE in Figure 11, are similar to those in Figure 3. Those are the LFQPOs present in those light curves during that exposure.

### 3.2. Spectral Properties

Studying the spectrum features sheds additional light on the nature of the outburst in addition to the temporal proper-



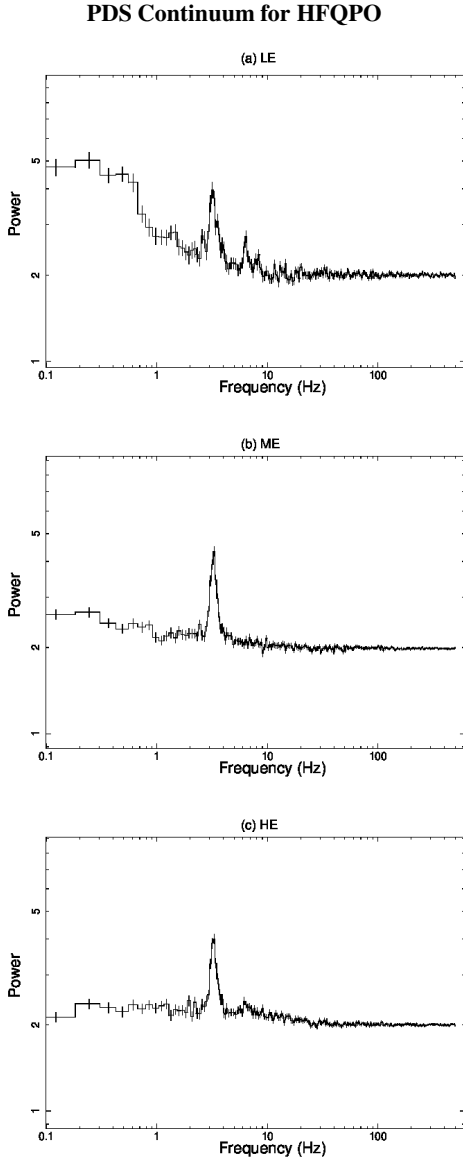


**Figure 11.** PDS continuum in the 0.1 – 500 Hz frequency range for (a) LE, (b) ME, and (c) HE bands. This is for the observation ID P0614374001 (exposure ID: P061437400101-20240304-01-0).

ties. We examined the source using the *Insight*-HXMT data that was accessible, for 14 exposures in total. The exposure IDs in Table 2’s first column have a ‘\*’ symbol next to them. We perform a thorough spectral study using HXMT data on this source for every consecutive days for the available data. Our spectrum investigation was initiated with MJD 60373.9. For spectral fitting, we have simultaneously analyzed LE+ME+HE in the 2 – 100 keV energy band (LE in 2–10, ME in 10–35, and HE in 27–100 keV) for all of the chosen exposure IDs.

First, we tried to model the spectrum with simple additive models `diskbb` and `power-law`. We also used the multiplicative `tbabs` (with `wilm` abundance, Wilms et al. (2000)) model to account for the interstellar ab-

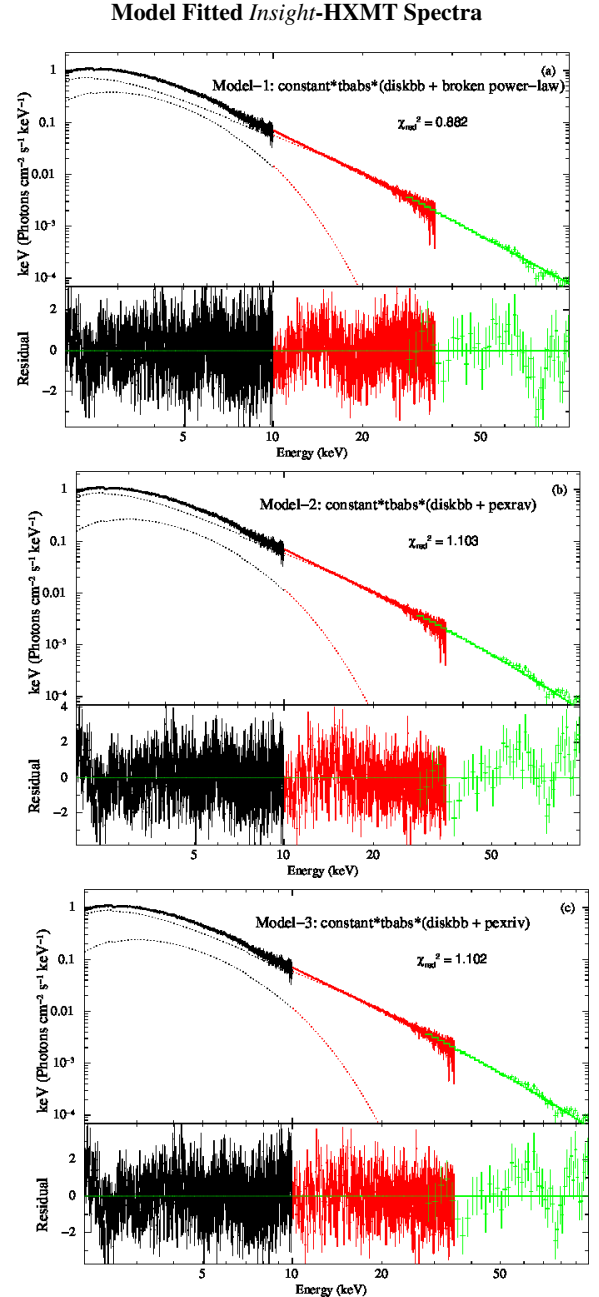


**Figure 12.** Best model fitted unfolded spectra for observation ID. P0614374001 (Exposure: P061437400101-20240304-01-01) using (a) Model-1, (b) Model-2, and (c) Model-3.

sorption. The model fitted unfolded spectrum is given in the Appendix section in Figure A.15. Although, the  $\chi^2/DOF$  value was acceptable, we noticed that the spectrum changes its slope above  $\sim 20$  keV. Thus, we replaced the power-law with the `broken power-law` model, which accounts for the change of slope after certain energy, called break energy ( $E_b$ ). In XSPEC, our model was expressed as `constant*tbabs(diskbb + broken powerlaw)`. The three distinct instruments (LE,

ME, and HE) are normalized using the constant. This model could fit the spectra for an acceptable  $\chi^2/DOF$  value ( $\sim 1$ ). These values can be found in column 11 of Table 5. Although this model fit was acceptable, there was a reflection nature in the spectrum. To account for that, we replaced the broken power-law model with the reflection model in neutral medium `pexrav`. With this model, using the model combination as `constant*tbabs(diskbb + pexrav)`, we also achieved the best fit. The  $\chi^2/DOF$  values can be found in column 11 of Table 6. We also checked the reflection component by using the reflection model `pexriv` which takes ionization into account. Thus `constant*tbabs(diskbb + pexriv)` is our Model-3 combination in XSPEC. We also achieved best fit using this combination. Here, we like to point out our approach using the Model 3. Except for 2 parameters, all the parameters of this model are the same as the `pexrav` model. While fitting with this model, we fixed the cut-off energy ( $E_{cut}$ ) of this model to the `pexrav` model. Also, we found while fitting that the disk temperature parameter (in units of Kelvin) was always taking its highest value, which is  $10^6$  Kelvin. Thus, for all the spectral fitting using this model, we freeze the value of this parameter to this highest value. The extra parameter that this model has over `pexrav` is the disk ionization parameter ( $\xi$ ), which is given as  $\xi = 4\pi F_{ion}/n$ , where  $n$  is the density of the reflector (Done et al. 1992) and  $F_{ion}$  is the irradiating flux in the 5 eV to 20 keV energy band. The best fitted parameters are given in Table 7 along with the fitting statistics. We find that the parameter variation of the `pexriv` model is similar to the `pexrav` model. In Figure 12(a-c), we show the model fitted best unfolded spectra using (a) Model-1, (b) Model-2, and (c) Model-3.

In Figure 13, we show the variations of some of the spectrally analyzed properties from both models. In panel (a), we show the variations of the hydrogen column density ( $N_H$ ) for both the model fittings (red filled-square for Model-1 and blue filled-square for Model-2). We notice that they show close variations within the error range throughout. While for Model-1,  $N_H$  varied between  $(4.3 - 6.5) \times 10^{22} \text{ cm}^{-2}$ , it varied in the range of  $(5.1 - 6.3) \times 10^{22} \text{ cm}^{-2}$  for Model-2 and in the range of  $(5 - 6.9) \times 10^{22}$  for Model-3. In panel (b), we show the variations in the inner-disk temperature ( $T_{in}$  in keV) for both models.  $T_{in}$  shows variation in the range of  $0.95 - 1.6 \text{ keV}$  for Model-1,  $1.3 - 2.1 \text{ keV}$  for Model-2, and  $0.9 - 2.1 \text{ keV}$  for Model-3. Since, the last exposure could not be fitted using Model-2, we think we have got the narrower variation using Model-2. In panel (c), we show the variations of photon indices. The red filled-square and hollow square represent  $\Gamma_1$  and  $\Gamma_2$  for the *broken power-law* model, where the blue and filled squares represent the  $\Gamma$  of the *pexrav* and the *pexriv* models. The energy break ( $E_b$ ) of the *broken power-law* model was  $19.2 \pm 0.3$  at the starting day and it decreased to  $8.54 \pm 0.3$  at the end of the analysis period. All the spectral parameters are given in Table 5, including fitting constants, needed to normalize simultaneous data in three bands. Similarly, all the spectral parameters are listed in Table 6 and 7, for the analysis using Model-2 and

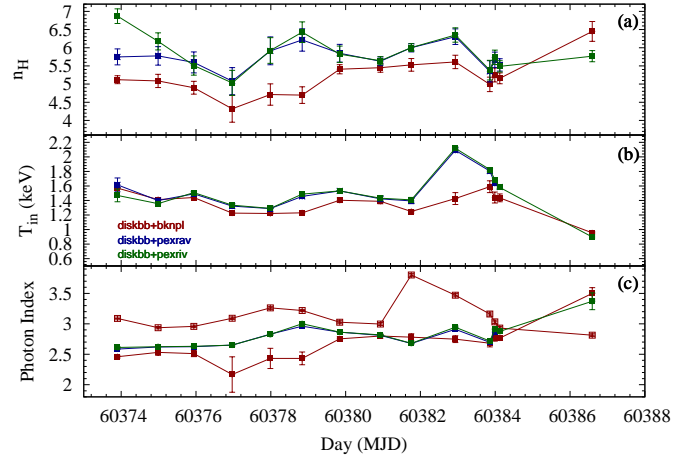


**Figure 13.** Variation of spectral model fitted properties. (a), (b), and (c) show the variation of hydrogen column density (in  $10^{22} \text{ cm}^{-2}$  unit), inner-disk temperature ( $T_{in}$  in keV), and photon index ( $\Gamma$ ) for all the three models with time. The red, blue, and green colors represent the properties for the *Model-1*, *Model-2*, and *Model-3*, respectively. In the (c) panel, we show the  $\Gamma_1$  and  $\Gamma_2$  of the *Model-1* using red color filled and hollow squares, respectively.

Model-3. For analysis with Model-2 and Model-3, we fixed the abundances to solar abundance and also varied the value of the inclination to a narrow range around  $30^\circ$  as reported by Mondal et al. (2024). However, on the last date of our analysis period, we found that although the fitting statistics were acceptable, the parameter space was unphysical. We tried to adjust the parameter space. However, the best fit was not achieved then. Thus we have left it blank in Table 6.

#### 4. DISCUSSIONS

The Galactic black hole Swift J151857.0-572147 started an outburst recently in March 2024. We have used *Insight-HXMT* data for our both timing and spectral studies from 2024 March 04 to 2024 March 17. Using the 0.01 sec time-binned light curves from the three instruments of HXMT (LE, ME, and HE), we studied the source's timing properties. We also searched for the energy dependence of LFQPOs by producing light curves in 7 different energy ranges within the HE band. Along with these, we searched for HFQPOs from all the light curves from LE, ME, and HE by making 1 ms time-binned light curves. We then examined the combined LE+ME+HE spectra in the 2 – 100 keV broad energy band to learn more about the spectral characteristics of this source using the spectra files from these three instruments.

For stellar-mass black holes, quasi-periodic oscillation is one of the most significant and frequent occurrences. We examined 186 exposures in total for this recently found source (62 for each of LE, ME, and HE). Nevertheless, incorrect light curve production occurred in 2 LE exposures. A total of 184 light curves for LE, ME, and HE were obtained.

The details are listed in Table 2. We discovered that QPO was not present in each of these light curves. The details on QPO properties are listed in Table 3. Over this brief analysis period, the QPO frequency has rapidly changed. Even in a single day, there was an increase in the QPO frequency ( $\nu_{qpo}$ ). The results section contains a general discussion of the QPO frequency's evolution. Type-C QPO nature is identified from the fluctuation of QPO frequency, (%)RMS, and  $Q$ -factor. One thing we would like to discuss here that the difference in RMS value (in Table 3) for LE, ME, and HE is due to the large variation in background counts in these three bands. As we can notice in Table 2, the background count in the HE band is almost equivalent to the source count in the HE band for this source. We recently studied the outburst properties of the BHC Swift J1727.8-1613 using HXMT data (Chatterjee et al. 2024). However, there was a great difference between the source and background count rates in all three bands. This is the case here for the LE and ME bands. For both sources, the same reduction method is used.

Even though the QPOs have been thoroughly examined in the literature, further modeling is necessary to understand their origin. Here, we want to concentrate on the physical scenario that explains how shock instabilities in advective flows near black holes (BHs) give rise to QPOs. According to Chakrabarti (1989), accretion onto BH is a transonic flow with the potential for numerous sonic locations. The companion's matter doesn't need to be exclusively Keplerian. A supply of matter with an angular momentum distribution that differs from the Keplerian one may exist. This is the sub-Keplerian component. Infalling matter with a smaller angular momentum component accretes over a free-fall timescale. At a certain distance from the black hole, this matter might nearly stop due to the counterbalance between the centrifugal force and gravitational force, undergo a shock transition, and form a post-shock region. Standing shocks form according to the flow properties (Chakrabarti 1989; Singh et al. 2022 and references therein). The spectral and temporal properties of BHs that have been seen can be effectively described by this method (Debnath et al. 2014; Mondal et al. 2014, Chatterjee et al. 2020, 2021, 2023). This shock may not be stable at the outer edge over time. There could be oscillations in the CENBOL boundary, which can be caused due to either of two reasons:

(i) According to Chakrabarti (1989), the satisfaction of the Rankine-Hugoniot condition makes the boundary of the shock stable and steady. However, if this condition is not satisfied, the shock could oscillate at the outer boundary to find local equilibrium. This could produce variabilities in the light curves.

(ii) Molteni et al. (1996) state that the presence of cooling may cause the shock to oscillate. QPOs emerge during the oscillation when the heating timescale and the cooling timescale caused by the Comptonization process match (see Chakrabarti et al. 2015).

The QPO frequency is given by,

$$\nu_{qpo} = \frac{c^3}{2GM_{BH}} \frac{1}{RX_s(X_s - 1)^{1/2}} Hz, \quad (1)$$

where the following are represented, respectively:  $c$ ,  $G$ ,  $M_{BH}$ ,  $X_s$ , and  $R$ ; these are the gravitational constant, the speed of light, the mass of the BH, the shock location, and the ratio of matter densities in post-shock to pre-shock regions ( $\rho_+/\rho_-$ ).

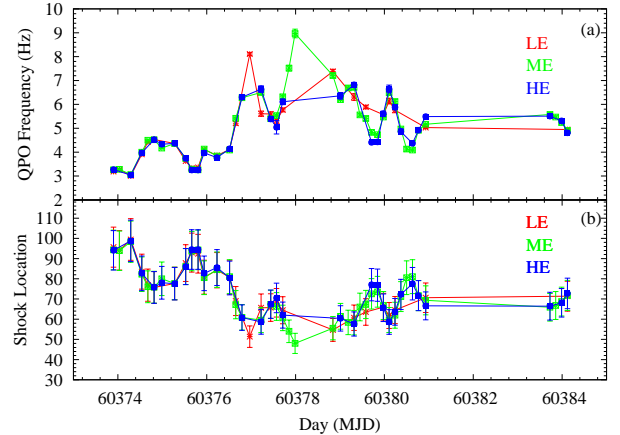


**Figure 14.** Variation of shock properties with time in accordance with  $\nu_{qpo}$ . In (a) the variation of  $\nu_{qpo}$  with time and in (b) we show the variations of the shock location ( $X_s$ ) with time.

We have already retrieved the QPO frequency ( $\nu_{qpo}$ ) from our timing analysis. We calculated the shock location during the outburst using the relation mentioned above. Chakrabarti et al. (2005) state that depending on the flow parameters causing shocks,  $X_s$  can be anywhere over  $10 r_s$ . When the spectral nature of an outburst is hard, the shock forms far away  $\sim 1000 r_s$ , and it gradually becomes small in the following days as cooling increases (Mondal et al. 2015). Based on Eq. 1, we discovered that during the beginning of the outburst, the shock was located at a distance of  $\sim 100 r_s$  from the BH (see Figure 14b). Then, as  $\nu_{qpo}$  increased, the shock moved inwards, suggesting cooling was in progress. After a few days, the shock became stable. Table 3 provides the values for the shock location (columns 11–13).

The light curve from MAXI/GSC was absent due to the proximity of another source in Cir X-1. Thus, from the HXMT extracted light curves and HR variations, we can roughly say that the source transitioned past its hard state at the start of our analysis period. It was at the end of its harder state (HS and HIMS). Our spectral analysis result also confirms this. From the variation of the photon index, we can say that the source was already in the end phase of its HIMS state and was transitioning towards its SIMS state. Our estimated shock location also agrees with this designation. At the start of our analysis period, shock was at a distance, which suggests the source has already transitioned past its hard state

and may be at the end of its hard intermediate state. Then the shock moved inward, suggesting now the source is making a transition towards the softer states via SIMS and SS. On several days, we did not notice any QPO signature from the start of our analysis to the end in any of the three bands. This could be because the infall and cooling timescales did not match for the shock. However, this could be also due to the data. For several days, QPO is only present in one of the three bands, whereas on some days it is present in two bands. We find that on the last day of our analysis period, the  $\Gamma$  became quite high, which suggests that the source transitioned into the soft state (SS) that day. Thus, we did not find QPO in any band on that day. The absence of QPOs and high  $\Gamma$  confirms the SS as inferred in Mondal et al. (2024) using *IXPE* and *NuSTAR* observations of the source.

We also found that high-frequency QPO was absent during the entire analysis duration of the outburst. Although the HFQPO phenomenon is not very common, its absence could be because the disk did not proceed very close to the compact object to produce variabilities with high frequency. Or, it could be due to the reason that the photon detection by HXMT instruments is not sufficient for this phenomenon. We also checked the energy dependence of LFQPOs in the HE band for those exposures in which LFQPO was present in the full energy band. The energy dependence of QPOs could give valuable insight into the origin of the QPO. In Ma et al. (2023) paper, they reported that LFQPO was present till very high energy, which suggested that the origin of the QPO could be from the precession of the jet. Examining all of those 31 exposures, we find that LFQPO was present till 48 keV, above which there is no prominent or weak QPO nature, either. In the 27 – 35 keV band, the nature of LFQPOs was stronger than in the 35 – 48 keV band. The shock was quite strong in the case of the BHC Swift J1727.8-1613 (Chatterjee et al. 2024), which could produce variabilities up to higher energies. However, for this source, the shock was not very big, which suggests that it has already cooled down by the process of inverse-Comptonization. Thus, it could only produce variabilities in hard photons up to 48 keV. This also supports our claim about the origin of the quasi-periodic oscillations, observed in the light curves.

Unlike the BHC Swift J1727.8-1613, this source has shown a very high value of hydrogen column density ( $N_H$ ), using both combinations of models.  $N_H$  varied in the range of  $(4.3 - 6.5) \times 10^{22} \text{ cm}^{-2}$  and  $(5.1 - 6.3) \times 10^{22} \text{ cm}^{-2}$  for Model-1 and Model-2, respectively. This is very high, considering Galactic black holes. This indicates some absorption local to the source, which could be due to the outflows from the disk or the presence of some blobs along the line of sight (see Neilsen & Homan, 2012; Mondal & Jithesh, 2023). To confirm this, we need a detailed study of the outflow/jet properties of the source.

## 5. SUMMARY AND CONCLUSIONS

We have studied the timing and spectral properties of the very first outburst of BHC Swift J1727.8-1613 in 2024. Using *Insight*-HXMT LE, ME, and HE exposure average light

curve data, we present the evolution of the light curve and its hardness ratio across our full analysis period. For our investigation, we selected the 7 observation IDs using the *Insight*-HXMT data, publicly available during the analysis. For timing analysis, we employed all of the exposures from those observation IDs, and for spectrum analysis, we employed selective exposures, respectively. We produced a power density spectrum and used 0.01 s time-binned light curves from the three HXMT instruments, i.e., LE, ME, and HE, to study the QPO properties. We used the Lorentzian model to obtain the QPO properties. We also studied energy-dependent QPO by producing HE light curves in seven different energy bands. We extracted the energy-dependent QPO properties in the same way we did for the LE, ME, and HE light curves in the full band. Apart from these, we also produced 0.001 s time-binned light curve to search for high-frequency QPOs. We employ LE + ME + HE spectrum files in the broad 2 – 100 keV energy band for spectral analysis. We found that the models i) `constant*tbabs*(diskbb + broken power-law)` and ii) `constant*tbabs*(diskbb + pexrav)` fit the spectra for the best statistics. Based on our investigation, we conclude that:

- i) The source was present in the intermediate state at the start of our analysis period and proceeded toward the soft state as the outburst progressed.
- ii) It was in the soft state at the last observation ID of our analysis period.
- iii) Type-C QPO was present in the intermediate state, which could be produced by the shock instability in the transonic accretion flow.
- iv) As the source transitioned to the soft state, we did not find any QPOs.
- v) LFQPOs were present up to 48 keV, above which we did not find the presence of LFQPO for all the exposures.
- vi) HFQPOs were absent during this analysis period.
- vii) As the shock was of intermediate strength, it could not produce variabilities up to very high energies. Thus, we only found QPOs up to 48 keV.
- viii) The hydrogen column density varied in the range of  $N_H \sim (4.3 - 6.9) \times 10^{22} \text{ cm}^{-2}$  in accord with the estimation by Mondal et al. (2024). This could be due to the presence of outflows from the disk or some blobs along the line of sight.

## 6. DATA AVAILABILITY

This work has made use of public data from several satellite/instrument archives and has made use of software from the HEASARC, which is developed and monitored by the Astrophysics Science Division at NASA/GSFC and the High Energy Astrophysics Division of the Smithsonian Astrophysical Observatory. This work made use of the data from the *Insight*-HXMT mission, a project funded by the China National Space Administration (CNSA) and the Chinese Academy of Sciences (CAS).

## 7. ACKNOWLEDGEMENTS

We thank Dr. Lian Tao of the Institute of High Energy Physics (IHEP), Chinese Academy of Sciences (CAS) for

publicizing the *Insight*-HXMT data by request. We also thank Prof. Mutsumi Sugizaki of the National Astronomical Observatory, Chinese Academy of Sciences (NAOC) for providing fruitful information about the absence of MAXI/GSC daily average light curve on the source. We sincerely thank Prof. John A. Tomsick of the Space Sciences Lab, University of California, Berkeley, USA for providing suggestions in the draft.

KC acknowledges support from the SWIFAR postdoctoral fund of Yunnan University. SPS and SM acknowledge the Ramanujan Fellowship (# RJF/2020/000113) by SERB-DST, Govt. of India for this research. CBS is supported by the National Natural Science Foundation of China under grant no. 12073021.

## REFERENCES

- Baglio, M. C., D’Avanzo, P., Ferro, M., Campana, S., Covino, S., 2024, *ATel*, 16506, 1
- Belloni, T., Homan, J., Casella, P., van der Klis, M., et al., 2005, *A&A*, 440, 207
- Bondi, H., 1952, *MNRAS*, 112, 195
- Bu, Q.-C., Li, Z.-S., Qu, J.-L., Belloni, T. M., Zhang, L., 2015, *ApJ*, 799, 2
- Burridge, B. J., Miller-Jones, J. C. A., Bahramian, A., Prabu, S., Carotenuto, F., et al., 2024, *ATel*, 16538, 1
- Carotenuto, F., Russell, T. D., JACKPOT Collaboration, 2024, *ATel*, 16518, 1
- Casella, P., Belloni, T., & Stella, L., 2005, *ApJ*, 629, 403
- Chakrabarti, S. K., 1989, *MNRAS*, 340, 7
- Chakrabarti, S. K., & Titarchuk, L. G., 1995, *ApJ*, 455, 623
- Chakrabarti, S. K., & Manickam, S. G., 2000, *ApJ*, 531, L41
- Chakrabarti, S. K., Acharya, K., & Molteni, D., 2004, *A&A*, 421, 1
- Chakrabarti, S. K., Nandi, A., Debnath, D., Sarkar, R., & Datta, B. G., 2005, preprint (arXiv:astro-ph/0508024)
- Chakrabarti, S. K., Debnath, D., Nandi, A., & Pal, P. S., 2008, *A&A*, 489, L41
- Chakrabarti, S. K., Mondal, S., & Debnath, D., 2015, *MNRAS*, 452, 3451
- Chatterjee, K., Debnath, D., Chatterjee, D., Jana, A., Chakrabarti, S. K., 2020, *MNRAS*, 493, 2452
- Chatterjee, K., Debnath, D., Chatterjee, D., Jana, A., et al., 2021, *Ap&SS*, 366, 63
- Chatterjee, K., Debnath, D., Nath, S. K., & Chang, H. -K., 2023, *ApJ*, 965, 55
- Chatterjee, K., Mondal, S., Singh, C. B., Sugizaki, M., 2024, *ApJS* (preprint: arXiv:2405.01498)
- Chen, Y., Cui, W., Li, W., et al. 2020, *Science China Physics, Mechanics, and Astronomy*, 63, 249505
- Cowie, F. J., Carotenuto, F., Fender, R. P., Heywood, I., Hughes, A. K., et al., 2024, *ATel*, 16503, 1
- Dauser, T., Garcia, J., Walton, D. J., et al., 2016, *A&A*, 590, A76
- Debnath, D., Chakrabarti, S.K., & Nandi, A., 2010, *A&A*, 520, A98
- Debnath, D., Chakrabarti, S. K., & Mondal, S., 2014, *MNRAS*, 440, L121
- Del Santo, M., Russell, T. D., Marino, A., & Motta, S., 2024, *ATel*, 16519, 1
- Done, C., Mulchaey, J. S., Mushotzky, R. F., & Arnaud, K. A., 1992, *ApJ*, 395, 275
- Frank, J., King, A., Raine, D., *Accretion Power in Astrophysics*, 2002, Cambridge University Press
- Hannikainen, D. C., Charles, P. A., van Zyl, L., et al. 2005, *MNRAS*, 357, 325
- Homan, J., Wijnands, R., van der Klis, M., Belloni, T., van Paradijs, J., KleinWolt, M., Fender, R., & Mendez, M., 2001, *ApJS*, 132, 377
- Ingram, A., Done, C., & Fragile, P. C., 2009, *MNRAS*, 397, L101
- Kennea, J. A., Lien, A. Y., D’Elia, V., Melandri, A., Page, K. L., et al., 2024, *ATel*, 16500, 1
- Leahy, D. A., et al., 1983, *ApJ*, 266, 160L
- Ma, X., Zhang, L., Bu, Q. C., Qu, J. L., Zhang, S. N., et al., 2023, *ApJ*, 948, 116
- McClintock, J.E., Narayan, R., & Steiner, J.F., 2013, *The Physics of Accretion onto Black Holes*, Space Sciences Series of ISSI, 49, 295
- Molteni, D., Sponholz, H., & Chakrabarti, S. K., 1996, *ApJ*, 457, 805
- Mondal, S., Debnath, D., & Chakrabarti, S. K., 2014, *ApJ*, 786, 4
- Mondal, S., Chakrabarti, S. K., & Debnath, D., 2015, *ApJ*, 798, 57
- Mondal, S., & Jithesh, V. 2023, *MNRAS*, 522, 2065
- Mondal, S., Suribhatla, S. P., Chatterjee, K., & Singh, C. B., 2024, (preprint: arXiv:2404.09643)
- Munoz-Darias, T., Motta, S., & Belloni, T. M., 2011, *MNRAS*, 410, 679
- Nandi, A., Debnath, D., Mandal, S., Chakrabarti, S. K., 2012, *A&A*, 542, 56
- Neilsen, J., & Homan, J. 2012, *ApJ*, 750, 27
- Paczynski, B., & Wiita, P., 1980, *A&A*, 88, 23
- Remillard, R. A., & McClintock, J. E., 2006, *ARA&A*, 44, 49
- Saikia, P., Russell, D. M., Baglio, M. C., Alabarta, K., Rout, S., et al., 2024, *ATel*, 16516, 1
- Sguera, V., 2024, *ATel*, 16524, 1
- Shakura, N. I., & Sunyaev, R. A., 1973, *A&A*, 24, 337
- Singh, C. B., Mondal, S., & Garofalo, D., 2022, *MNRAS*, 510, 807
- Stella, L., Vietri, M., & Morsink, S. M., 1999, *ApJ*, 524, L63

- Sunyaev, R. A., & Titarchuk, L. G., 1980, *A&A*, 500, 167
- Sunyaev, R. A., & Titarchuk, L. G., 1985, *A&A*, 143, 374
- Tagger, M., & Pellat, R., 1999, *A&A*, 349, 1003
- Tetarenko, B. E., Sivakoff, G. R., Heinke, C. O., & Gladstone, J. C., 2016, *ApJS*, 222, 15
- Titarchuk, L., Lapidus, I., & Muslimov, A., 1998, *ApJ*, 499, 315
- van der Klis, M., 1989, *Annu. Rev. Astron. Astrophys.*, 27, 517
- Wilms, J., Allen, A., & McCray, R., 2000, *ApJ*, 542, 914
- Zhang, S. -N., et al., 2020, *Science China Physics, Mechanics, and Astronomy* 63, 249502
- Zhang, G. B., Bernardini, F., Russell, D. M., Gelfand, J. D., Lasota, J.-P. et al., 2019, *ApJ*, 876, 5

**Table 2.** Time and Count Rates of all the HXMT Exposures. Column 1 represents the Exposure IDs, taken for this complete analysis. Column 2 and 3 represent the start and end MJDs of those exposures respectively. Column 4 represents the average MJD for those exposure IDs. Columns 5, 6, & 7 represent source count rate in LE, ME, and HE bands Columns 8, 9, & 10 represent background count rate in LE, ME, and HE bands

Exposure	MJD			Source Count Rate			Background Count Rate		
ID	Start	Stop	Average	LE	ME	HE	LE	ME	HE
(1)	(4)	(5)	(6)	(7)	(8)	(9)	(10)	(11)	(12)
P061437400101-20240304-01-01*	60373.8396	60373.9655	60373.9025	536.58	138.35	570.52	10.86	23.95	404.71
P061437400102-20240304-01-01	60373.9655	60374.1042	60374.0348	580.17	156.85	624.12	10.96	24.83	523.82
P061437400103-20240305-02-01	60374.1042	60374.4766	60374.2904	623.90	159.03	567.25	11.07	23.00	375.57
P061437400104-20240305-02-01	60374.4766	60374.6045	60374.5406	637.14	140.78	522.86	10.54	22.75	357.61
P061437400105-20240305-02-01	60374.6045	60374.7440	60374.6742	662.66	140.50	585.67	10.31	25.13	442.21
P061437400106-20240305-02-01	60374.7440	60374.8851	60374.8145	644.42	132.14	541.91	10.74	21.73	404.61
P061437400107-20240305-02-01*	60374.8851	60375.0928	60374.9889	632.28	130.30	552.83	10.73	24.15	397.43
P061437400201-20240306-01-01	60375.0928	60375.4647	60375.2787	622.66	126.47	523.01	10.95	22.51	380.94
P061437400202-20240306-01-01	60375.4647	60375.5929	60375.5288	595.72	130.94	535.99	10.65	22.87	382.38
P061437400203-20240306-01-01	60375.5929	60375.7329	60375.6629	600.56	139.07	621.86	10.96	25.96	423.93
P061437400204-20240306-01-01	60375.7329	60375.8736	60375.8032	599.74	139.67	575.39	10.65	22.71	397.88
P061437400205-20240306-01-01*	60375.8736	60376.0117	60375.9426	595.50	131.44	555.10	11.40	24.49	403.45
P061437400206-20240307-02-01	60376.0117	60376.4527	60376.2322	608.29	133.40	535.65	11.06	22.87	377.09
P061437400207-20240307-02-01	60376.4527	60376.5813	60376.5170	621.09	129.42	522.51	11.19	22.66	366.92
P061437400208-20240307-02-01	60376.5813	60376.7219	60376.6516	604.54	113.97	550.91	10.61	24.82	436.03
P061437400209-20240307-02-01	60376.7219	60376.8622	60376.7921	638.58	108.06	500.53	10.37	22.94	398.94
P061437400210-20240307-02-01*	60376.8622	60377.0718	60376.9670	666.77	98.46	493.26	11.88	23.53	425.96
P061437400301-20240308-01-01	60377.0718	60377.3772	60377.2245	633.28	103.44	473.36	10.53	21.98	375.15
P061437400302-20240308-01-01	60377.3772	60377.5025	60377.4399	669.41	117.44	481.87	11.93	23.36	374.84
P061437400303-20240308-01-01	60377.5025	60377.6373	60377.5699	625.12	113.95	518.43	11.07	27.79	396.08
P061437400304-20240308-01-01	60377.6373	60377.7815	60377.7094	605.70	106.46	510.03	10.22	22.89	410.33
P061437400305-20240308-01-01	60377.7815	60377.9197	60377.8506	600.03	92.76	473.50	10.47	22.67	391.08
P061437400306-20240308-01-01*	60377.9197	60378.0588	60377.9892	627.36	92.00	472.99	10.61	23.77	419.09
P061437400307-20240309-02-01	60378.0588	60378.3653	60378.2121	651.44	82.46	416.10	10.34	21.32	372.58
P061437400308-20240309-02-01	60378.3653	60378.4909	60378.4281	-	77.33	409.98	-	24.98	355.93
P061437400309-20240309-02-01	60378.4909	60378.6258	60378.5583	598.49	79.97	446.97	11.36	25.21	366.72
P061437400310-20240309-02-01	60378.6258	60378.7701	60378.6980	642.67	87.64	460.32	10.32	23.54	421.21
P061437400311-20240309-02-01*	60378.7701	60378.9082	60378.8391	613.15	98.77	473.44	10.27	23.16	387.30
P061437400312-20240309-02-01	60378.9082	60379.1171	60379.0127	600.63	105.11	489.30	10.49	23.10	402.28
P061437400401-20240310-01-01	60379.1171	60379.2518	60379.1845	602.94	96.22	455.29	10.20	22.20	375.02
P061437400402-20240310-01-01	60379.2518	60379.3831	60379.3175	565.28	93.30	451.50	10.00	22.68	357.27
P061437400403-20240310-01-01	60379.3831	60379.5146	60379.4489	-	108.09	467.63	-	26.14	357.47
P061437400404-20240310-01-01	60379.5146	60379.6460	60379.5803	555.07	115.94	515.31	11.10	27.98	416.68
P061437400405-20240310-01-01	60379.6460	60379.7775	60379.7118	537.59	113.94	521.13	10.30	23.27	415.00
P061437400406-20240310-01-01*	60379.7775	60379.9090	60379.8432	509.38	104.94	503.53	10.25	24.60	378.08
P061437400407-20240310-01-01	60379.9090	60380.0405	60379.9748	517.66	97.23	502.49	10.53	23.50	405.01

Table 2 – continued from previous page

Exposure ID (1)	MJD			Source Count Rate			Background Count Rate		
	Start (4)	Stop (5)	Average (6)	LE (7)	ME (8)	HE (9)	LE (10)	ME (11)	HE (12)
P061437400408-20240311-02-01	60380.0405	60380.1721	60380.1063	527.40	90.35	465.21	10.32	21.46	376.86
P061437400409-20240311-02-01	60380.1721	60380.3036	60380.2379	571.07	106.01	462.14	9.93	22.41	360.21
P061437400410-20240311-02-01	60380.3036	60380.4352	60380.3694	548.30	115.14	474.22	10.07	22.07	373.48
P061437400411-20240311-02-01	60380.4352	60380.5668	60380.5010	580.27	134.88	525.68	11.17	29.07	386.17
P061437400412-20240311-02-01	60380.5668	60380.6983	60380.6325	462.08	106.48	537.55	9.94	25.56	420.90
P061437400413-20240311-02-01	60380.6983	60380.8299	60380.7641	477.94	97.35	493.75	10.20	22.13	396.88
P061437400414-20240311-02-01*	60380.8299	60381.0332	60380.9315	474.07	96.15	498.83	10.35	23.93	404.79
P061437400501-20240312-01-01	60381.4266	60381.5539	60381.4903	483.34	68.63	433.63	10.76	26.38	405.46
P061437400502-20240312-01-01	60381.5539	60381.6855	60381.6197	482.73	64.80	445.23	10.16	24.11	424.39
P061437400503-20240312-01-01*	60381.6855	60381.8286	60381.7571	537.66	80.44	417.55	10.13	21.57	402.64
P061437400601-20240313-01-01	60382.4164	60382.5817	60382.4990	510.02	79.82	443.41	10.98	26.42	397.53
P061437400602-20240313-01-01	60382.5817	60382.7243	60382.6530	516.28	82.24	437.49	9.78	23.70	412.44
P061437400603-20240313-01-01	60382.7243	60382.8624	60382.7933	506.55	88.41	435.97	9.95	23.59	391.56
P061437400604-20240313-01-01*	60382.8624	60383.0022	60382.9323	501.54	92.93	460.78	10.00	24.10	401.87
P061437400605-20240314-02-01	60383.0022	60383.1339	60383.0681	446.42	67.57	428.66	10.19	21.78	380.04
P061437400606-20240314-02-01	60383.1339	60383.2656	60383.1997	441.60	69.75	419.85	9.98	21.97	368.76
P061437400607-20240314-02-01	60383.2656	60383.3973	60383.3314	430.38	75.95	434.04	9.76	23.01	355.99
P061437400608-20240314-02-01	60383.3973	60383.5291	60383.4632	494.91	100.00	482.17	11.36	28.54	445.78
P061437400609-20240314-02-01	60383.5291	60383.6608	60383.5949	473.40	97.84	479.17	9.87	24.27	428.51
P061437400610-20240314-02-01	60383.6608	60383.7925	60383.7266	470.76	107.58	473.73	9.83	22.89	400.49
P061437400611-20240314-02-01*	60383.7925	60383.9205	60383.8565	442.65	94.15	520.03	10.68	24.74	411.57
P061437400612-20240314-02-01*	60383.9205	60384.0559	60383.9882	405.67	84.88	471.21	10.46	22.74	395.89
P061437400613-20240315-03-01*	60384.0559	60384.1876	60384.1217	385.96	84.14	459.38	10.01	22.73	376.74
P061437400614-20240315-03-01	60384.1876	60384.3977	60384.2927	408.51	80.65	438.74	9.89	22.18	366.30
P061437400801-20240317-01-01*	60386.5069	60386.6783	60386.5926	265.65	36.99	421.11	9.68	22.76	404.34
P061437400802-20240317-01-01	60386.6783	60386.9141	60386.7962	256.75	43.10	440.27	9.88	24.65	422.77



**Table 3.** Properties estimated using timing analysis of HE Light Curves. In column 1, we have listed the MJD-60370 (to save space) of the exposure IDs we used. Columns 2, 3, & 4 represent the QPO frequency in LE, ME, and HE energy bands respectively. Columns 5, 6, & 7 represent the Q-values of QPOs in LE, ME, and HE energy bands respectively. Columns 8, 9, & 10 represent the QPO RMS (%) in LE, ME, and HE energy bands respectively. Columns 11, 12, & 13 represent the shock location in LE, ME, and HE energy bands respectively.

Time (MJD)	QPO Frequency (Hz)			Q-Value			RMS			Shock Location ( $X_s$ )		
	LE	ME	HE	LE	ME	HE	LE	ME	HE	LE	ME	HE
(1)	(2)	(3)	(4)	(5)	(6)	(7)	(8)	(9)	(10)	(11)	(12)	(13)
3.90	3.19 ± 0.02	3.25 ± 0.08	3.26 ± 0.01	9.1 ± 1.3	9.0 ± 0.5	9.0 ± 0.7	4.3 ± 0.4	10.8 ± 0.4	5.8 ± 0.3	95.6 ± 9.9	94.2 ± 9.7	94.0 ± 9.7
4.03	3.26 ± 0.04	3.27 ± 0.02	-	7.1 ± 1.5	7.1 ± 0.6	-	4.1 ± 0.5	9.7 ± 0.5	-	94.0 ± 9.7	93.9 ± 9.7	-
4.28	3.00 ± 0.00	3.05 ± 0.09	3.03 ± 0.07	8.1 ± 0.8	6.5 ± 0.3	7.0 ± 0.3	3.4 ± 0.2	9.6 ± 0.2	6.5 ± 0.1	99.4 ± 10.3	98.3 ± 10.2	98.7 ± 10.2
4.53	3.91 ± 0.04	4.00 ± 0.03	3.97 ± 0.04	6.5 ± 1.4	4.6 ± 0.5	4.1 ± 0.4	3.5 ± 0.4	11.2 ± 0.7	7.3 ± 0.5	83.5 ± 8.6	82.2 ± 8.5	82.6 ± 8.5
4.67	4.42 ± 0.03	4.50 ± 0.02	-	8.5 ± 1.3	6.1 ± 0.5	-	3.6 ± 0.3	11.5 ± 0.6	-	76.8 ± 7.9	76.0 ± 7.8	-
4.81	4.53 ± 0.04	4.51 ± 0.02	4.53 ± 0.02	7.9 ± 1.6	5.7 ± 0.3	6.6 ± 0.4	3.7 ± 0.4	12.4 ± 0.5	6.5 ± 0.3	75.7 ± 7.8	75.8 ± 7.8	75.7 ± 7.8
4.98	-	4.17 ± 0.02	4.32 ± 0.02	-	6.2 ± 0.3	8.8 ± 1.0	-	12.6 ± 0.4	6.1 ± 0.4	-	80.0 ± 8.3	78.0 ± 8.0
5.27	4.36 ± 0.02	4.36 ± 0.08	4.36 ± 0.09	9.4 ± 1.2	7.6 ± 0.3	7.6 ± 0.4	3.6 ± 0.2	12.0 ± 0.2	6.3 ± 0.2	77.6 ± 8.0	77.6 ± 8.0	77.5 ± 8.0
5.52	3.63 ± 0.02	3.74 ± 0.02	3.74 ± 0.02	10.6 ± 1.8	8.6 ± 0.8	7.4 ± 0.7	4.0 ± 0.4	11.7 ± 0.7	7.0 ± 0.4	87.7 ± 9.1	86.0 ± 8.9	86.0 ± 8.9
5.66	3.32 ± 0.03	3.28 ± 0.02	3.25 ± 0.02	6.6 ± 1.3	7.4 ± 0.6	12. ± 2.8	3.9 ± 0.4	10.9 ± 0.6	5.3 ± 0.8	92.9 ± 9.6	93.7 ± 9.7	94.4 ± 9.8
5.80	3.35 ± 0.03	3.25 ± 0.02	3.25 ± 0.02	7.0 ± 1.4	4.4 ± 0.2	4.6 ± 0.3	3.6 ± 0.4	11.8 ± 0.5	6.4 ± 0.3	92.4 ± 9.5	94.2 ± 9.7	94.4 ± 9.8
5.94	4.11 ± 0.03	4.13 ± 0.02	3.97 ± 0.02	8.9 ± 2.3	7.0 ± 0.2	11.3 ± 1.6	3.9 ± 0.6	11.5 ± 0.4	5.7 ± 0.5	80.7 ± 8.3	80.5 ± 8.3	82.6 ± 8.5
6.23	3.85 ± 0.02	3.83 ± 0.02	3.76 ± 0.02	6.7 ± 0.9	6.0 ± 0.2	5.6 ± 0.2	3.8 ± 0.3	11.6 ± 0.3	6.7 ± 0.1	84.2 ± 8.7	84.5 ± 8.7	85.5 ± 8.8
6.51	4.11 ± 0.02	4.09 ± 0.02	4.13 ± 0.02	16.4 ± 3.9	12.7 ± 1.5	9.0 ± 1.3	3.3 ± 0.5	11.1 ± 0.9	6.1 ± 0.6	80.7 ± 8.3	81.0 ± 8.4	80.4 ± 8.3
6.65	5.21 ± 0.08	5.42 ± 0.03	-	5.0 ± 1.3	4.2 ± 0.4	-	3.9 ± 0.5	13.6 ± 0.9	-	68.9 ± 7.1	67.1 ± 6.9	-
6.79	-	6.28 ± 0.02	6.30 ± 0.05	-	7.5 ± 0.8	6.2 ± 1.0	-	11.0 ± 0.7	5.2 ± 0.5	-	60.9 ± 6.3	60.7 ± 6.3
6.96	8.10 ± 0.06	-	-	5.9 ± 0.8	-	-	3.8 ± 0.3	-	-	51.3 ± 5.3	-	-
7.22	5.61 ± 0.15	6.50 ± 0.09	6.63 ± 0.15	4.6 ± 1.4	2.3 ± 0.2	1.9 ± 0.3	2.7 ± 0.5	13.9 ± 0.8	6.7 ± 0.6	65.6 ± 6.8	59.5 ± 6.1	58.6 ± 6.0
7.44	5.59 ± 0.09	5.40 ± 0.03	5.38 ± 0.08	6.5 ± 2.4	9.3 ± 1.7	4.8 ± 1.0	3.8 ± 0.8	10.6 ± 1.3	7.1 ± 0.9	65.7 ± 6.8	67.3 ± 6.9	67.4 ± 6.9
7.57	5.30 ± 0.09	5.53 ± 0.06	5.03 ± 0.21	17.6 ± 17.	4.4 ± 0.7	1.4 ± 0.5	2.2 ± 1.1	13.5 ± 1.3	10.0 ± 2.0	68.1 ± 7.0	66.2 ± 6.8	70.5 ± 7.3
7.71	5.76 ± 0.08	6.32 ± 0.06	6.11 ± 0.14	6.1 ± 1.6	3.6 ± 0.5	3.1 ± 0.6	3.4 ± 0.5	12.7 ± 1.0	6.0 ± 0.7	64.4 ± 6.6	60.6 ± 6.2	62.0 ± 6.4
7.85	-	7.51 ± 0.16	-	-	3.3 ± 0.5	-	-	12.9 ± 1.3	-	-	54.0 ± 5.6	-
7.98	-	8.97 ± 0.18	-	-	3.6 ± 0.9	-	-	11.6 ± 1.7	-	-	48.0 ± 4.9	-
8.21	-	-	-	-	-	-	-	-	-	-	-	-
8.42	-	-	-	-	-	-	-	-	-	-	-	-
8.55	-	-	-	-	-	-	-	-	-	-	-	-
8.69	-	-	-	-	-	-	-	-	-	-	-	-
8.83	7.38 ± 0.09	7.21 ± 0.09	-	13.6 ± 6.8	4.0 ± 0.7	-	2.1 ± 0.6	11.2 ± 1.2	-	54.6 ± 5.6	55.5 ± 5.7	-
9.01	-	6.19 ± 0.03	6.36 ± 0.15	-	7.7 ± 1.2	3.8 ± 1.0	-	9.5 ± 0.9	5.7 ± 0.9	-	61.4 ± 6.3	60.3 ± 6.2
9.18	-	6.69 ± 0.09	-	-	5.0 ± 1.1	-	-	9.7 ± 1.3	-	-	58.3 ± 6.0	-
9.31	6.30 ± 0.13	6.71 ± 0.07	6.82 ± 0.13	5.5 ± 2.2	5.9 ± 1.3	4.5 ± 0.9	3.1 ± 0.7	10.4 ± 1.4	6.1 ± 0.7	60.7 ± 6.2	58.2 ± 6.0	57.6 ± 5.9
9.44	-	5.55 ± 0.04	-	-	11.5 ± 3.3	-	-	9.8 ± 1.8	-	-	66.0 ± 6.8	-
9.58	5.88 ± 0.07	5.40 ± 0.13	-	13.3 ± 6.9	4.5 ± 1.2	-	3.0 ± 0.9	10.5 ± 1.6	-	63.5 ± 6.5	67.2 ± 6.9	-
9.71	-	4.82 ± 0.09	4.40 ± 0.03	-	2.9 ± 0.5	7.7 ± 1.2	-	10.7 ± 1.1	4.9 ± 0.4	-	72.5 ± 7.5	77.0 ± 7.9

Continued on next page



**Table 4.** Properties from Energy Dependent Timing Analysis. In column 1, we have listed the MJD of the exposure IDs we used. Columns 2, 3, & 4 represent the QPO frequency,  $Q$ -value, and RMS (%), respectively in 27-35 keV energy band. Columns 5, 6, & 7 represent the QPO frequency,  $Q$ -value, and RMS (%), respectively in 35-48 keV energy band.

Time	27-35 keV			35-48 keV		
(MJD)	Frequency (Hz)	$Q$ -Value	RMS (%)	Frequency (Hz)	$Q$ -Value	RMS (%)
(1)	(2)	(3)	(4)	(5)	(6)	(7)
60373.9025	3.27 ± 0.01	8.60 ± 0.67	5.93 ± 0.30	3.25 ± 0.01	8.55 ± 0.90	4.59 ± 0.31
60374.2904	3.06 ± 0.09	6.65 ± 0.34	6.05 ± 0.17	3.02 ± 0.01	6.56 ± 0.42	4.93 ± 0.20
60374.5406	3.93 ± 0.03	4.73 ± 0.51	6.88 ± 0.48	4.01 ± 0.06	4.01 ± 0.72	5.60 ± 0.59
60374.8145	4.50 ± 0.02	5.76 ± 0.51	6.46 ± 0.36	4.54 ± 0.03	6.13 ± 0.74	5.15 ± 0.38
60374.9889	4.32 ± 0.01	10.2 ± 1.22	5.74 ± 0.45	4.31 ± 0.02	10.0 ± 1.63	5.02 ± 0.51
60375.2787	4.36 ± 0.01	8.54 ± 0.50	5.93 ± 0.21	4.34 ± 0.01	7.75 ± 0.55	5.14 ± 0.23
60375.5288	3.80 ± 0.02	5.93 ± 0.74	7.01 ± 0.55	3.77 ± 0.04	7.11 ± 1.47	4.86 ± 0.63
60375.6629	3.22 ± 0.02	10.3 ± 1.67	5.92 ± 0.68	3.19 ± 0.03	9.38 ± 2.20	4.85 ± 0.74
60375.8032	3.26 ± 0.02	4.28 ± 0.39	6.15 ± 0.36	3.22 ± 0.02	5.27 ± 0.60	5.06 ± 0.36
60375.9426	3.96 ± 0.02	9.65 ± 1.64	5.29 ± 0.58	3.98 ± 0.03	9.25 ± 1.93	4.89 ± 0.64
60376.2322	3.79 ± 0.01	5.65 ± 0.33	6.31 ± 0.23	3.82 ± 0.01	6.16 ± 0.49	5.07 ± 0.25
60376.5170	4.13 ± 0.03	8.42 ± 1.54	6.00 ± 0.70	4.13 ± 0.02	13.7 ± 2.75	4.71 ± 0.62
60376.7921	6.21 ± 0.06	5.04 ± 0.86	5.58 ± 0.56	6.51 ± 0.14	3.51 ± 0.89	5.00 ± 0.76
60377.2245	6.84 ± 0.14	2.22 ± 0.38	6.48 ± 0.70	–	–	–
60377.4399	5.43 ± 0.04	7.98 ± 1.52	6.81 ± 0.81	5.43 ± 0.06	7.86 ± 2.16	5.54 ± 0.95
60377.5699	5.19 ± 0.18	2.22 ± 0.62	9.20 ± 1.51	5.47 ± 0.21	3.93 ± 1.81	5.58 ± 1.5
60377.7094	6.55 ± 0.11	3.92 ± 0.87	5.78 ± 0.75	–	–	–
60379.3175	6.68 ± 0.20	2.81 ± 0.84	6.19 ± 1.04	6.72 ± 0.24	2.63 ± 0.89	5.91 ± 1.1
60379.7118	4.68 ± 0.12	2.96 ± 0.77	5.47 ± 0.77	5.21 ± 0.20	1.77 ± 0.47	6.30 ± 0.91
60379.8432	4.45 ± 0.02	11.7 ± 1.84	5.27 ± 0.54	4.43 ± 0.04	7.91 ± 1.69	5.03 ± 0.68
60379.9748	5.59 ± 0.12	5.53 ± 2.08	4.71 ± 1.07	5.82 ± 0.13	6.53 ± 2.86	4.31 ± 1.0
60380.1063	6.53 ± 0.10	4.03 ± 0.82	6.13 ± 0.74	6.21 ± 0.19	2.54 ± 0.75	5.85 ± 0.94
60380.2379	5.82 ± 0.26	1.41 ± 0.35	7.56 ± 1.04	5.72 ± 0.21	2.90 ± 1.02	4.75 ± 0.97
60380.3694	5.04 ± 0.08	4.75 ± 1.21	6.03 ± 0.95	–	–	–
60380.6325	4.30 ± 0.03	10.4 ± 2.30	4.73 ± 0.65	4.35 ± 0.08	5.64 ± 1.76	4.56 ± 0.86
60380.7641	4.96 ± 0.03	7.87 ± 1.00	5.54 ± 0.43	4.97 ± 0.03	9.37 ± 1.77	4.37 ± 0.49
60380.9315	5.35 ± 0.11	4.38 ± 1.29	5.53 ± 0.95	–	–	–
60383.7266	5.58 ± 0.07	5.52 ± 1.09	5.03 ± 0.58	5.65 ± 0.11	4.55 ± 1.32	4.52 ± 0.77
60383.9882	5.29 ± 0.05	8.53 ± 2.06	4.77 ± 0.70	5.18 ± 0.12	5.69 ± 2.38	3.50 ± 0.91
60384.2927	4.92 ± 0.04	8.06 ± 1.58	4.98 ± 0.60	4.98 ± 0.08	6.14 ± 1.90	4.25 ± 0.78

**Table 5.** Properties from spectral analysis using Model-1. Column 1 represents the MJD of those respective Exposure IDs for which we have performed spectral analysis. Column 2 gives the values of the hydrogen column densities ( $N_H$ ) of those analyzed exposures. Columns 3 & 4 give the values of the parameters from the *diskbb* model. Columns 5-8 give the values of the parameters from the *broken power-law* model. Columns 9 & 10 give the values of the constants needed to achieve simultaneous broadband fitting. Column 11 gives the values of the  $\chi^2/DOF$  for each fitting.

Time	TBabs	diskbb		broken power-law				Fitting constants		Fitting Stat
MJD	$N_H$	$T_{in}$ (keV)	Norm	$\Gamma_1$	$E_b$ (keV)	$\Gamma_2$	Norm	Constant1	Constant2	$\chi^2/DOF$
(1)	(2)	(3)	(4)	(5)	(6)	(7)	(8)	(9)	(10)	(11)
60373.9025	$5.11 \pm 0.10$	$1.57 \pm 8.7E - 3$	$145.4 \pm 7.5$	$2.45 \pm 2.3E - 2$	$19.2 \pm 0.3$	$3.08 \pm 2.2E - 2$	$15.4 \pm 1.1$	$1.10 \pm 1.0E - 2$	$1.15 \pm 1.9E - 2$	1242.96/1410
60374.9889	$5.08 \pm 0.18$	$1.41 \pm 1.3E - 2$	$278.0 \pm 22.8$	$2.53 \pm 4.7E - 2$	$15.1 \pm 0.4$	$2.93 \pm 1.8E - 2$	$19.8 \pm 2.5$	$1.01 \pm 1.2E - 2$	$0.97 \pm 2.0E - 2$	1238.56/1410
60375.9426	$4.89 \pm 0.17$	$1.44 \pm 1.9E - 2$	$221.6 \pm 23.1$	$2.51 \pm 4.9E - 2$	$14.4 \pm 0.5$	$2.95 \pm 2.1E - 2$	$18.5 \pm 2.3$	$1.04 \pm 1.3E - 2$	$1.04 \pm 2.5E - 2$	1188.51/1410
60376.9670	$4.31 \pm 0.36$	$1.22 \pm 1.6E - 2$	$844.3 \pm 103$	$2.16 \pm 0.24$	$10.7 \pm 0.2$	$3.09 \pm 2.2E - 2$	$7.16 \pm 4.9$	$0.96 \pm 2.4E - 2$	$0.91 \pm 3.4E - 2$	1186.14/1410
60377.9892	$4.71 \pm 0.29$	$1.22 \pm 1.1E - 2$	$754.7 \pm 74.8$	$2.43 \pm 0.16$	$11.4 \pm 0.2$	$3.26 \pm 2.4E - 2$	$11.8 \pm 4.4$	$1.00 \pm 1.8E - 2$	$0.89 \pm 4.2E - 2$	1204.31/1410
60378.8391	$4.69 \pm 0.22$	$1.23 \pm 1.2E - 2$	$590.1 \pm 60.8$	$2.43 \pm 0.13$	$11.0 \pm 0.2$	$3.21 \pm 1.8E - 2$	$14.2 \pm 3.4$	$0.95 \pm 1.3E - 2$	$1.06 \pm 2.6E - 2$	1266.20/1410
60379.8432	$5.40 \pm 0.12$	$1.40 \pm 3.1E - 2$	$135.8 \pm 20.1$	$2.75 \pm 3.2E - 2$	$14.5 \pm 0.8$	$3.02 \pm 2.5E - 2$	$27.9 \pm 2.0$	$1.01 \pm 1.2E - 2$	$1.15 \pm 3.1E - 2$	1234.25/1410
60380.9315	$5.45 \pm 0.12$	$1.38 \pm 3.3E - 2$	$128.9 \pm 20.2$	$2.79 \pm 3.3E - 2$	$14.2 \pm 1.1$	$2.99 \pm 2.5E - 2$	$27.9 \pm 2.0$	$1.03 \pm 1.2E - 2$	$0.96 \pm 3.1E - 2$	1184.85/1410
60381.7571	$5.52 \pm 0.17$	$1.24 \pm 2.3E - 2$	$338.8 \pm 48.6$	$2.78 \pm 5.6E - 2$	$11.8 \pm 0.1$	$3.80 \pm 2.7E - 2$	$27.5 \pm 3.4$	$0.96 \pm 1.2E - 2$	$0.93 \pm 3.9E - 2$	1270.61/1410
60382.9323	$5.60 \pm 0.18$	$1.42 \pm 8.1E - 2$	$102.4 \pm 34.0$	$2.74 \pm 5.5E - 2$	$12.0 \pm 0.3$	$3.47 \pm 2.6E - 2$	$29.2 \pm 3.2$	$0.94 \pm 1.4E - 2$	$1.06 \pm 3.7E - 2$	1243.06/1410
60383.8565	$4.99 \pm 0.19$	$1.58 \pm 8.1E - 2$	$68.84 \pm 18.6$	$2.68 \pm 5.9E - 2$	$13.1 \pm 0.7$	$3.16 \pm 3.2E - 2$	$21.0 \pm 2.4$	$0.99 \pm 1.8E - 2$	$1.32 \pm 8.6E - 2$	1299.35/1410
60383.9882	$5.25 \pm 0.19$	$1.44 \pm 7.5E - 2$	$80.31 \pm 24.8$	$2.76 \pm 5.4E - 2$	$13.2 \pm 1.2$	$3.03 \pm 2.7E - 2$	$23.2 \pm 2.6$	$1.02 \pm 1.9E - 2$	$1.03 \pm 3.4E - 2$	1312.79/1410
60384.1217	$5.15 \pm 0.14$	$1.43 \pm 5.4E - 2$	$75.04 \pm 17.6$	$2.76 \pm 3.9E - 2$	$14.4 \pm 1.6$	$2.93 \pm 2.7E - 2$	$21.9 \pm 1.8$	$1.04 \pm 1.5E - 2$	$0.99 \pm 3.1E - 2$	1188.29/1410
60386.5926	$6.44 \pm 0.27$	$0.95 \pm 1.7E - 2$	$757.6 \pm 117$	$3.50 \pm 9.3E - 2$	$8.54 \pm 0.3$	$2.81 \pm 2.3E - 2$	$34.5 \pm 6.8$	$1.05 \pm 2.3E - 2$	$1.07 \pm 5.3E - 2$	1344.08/1410

**Table 6.** Properties from spectral analysis using Model-2. Column 1 represents the MJD of those respective Exposure IDs for which we have performed spectral analysis. Column 2 gives the values of hydrogen column densities ( $N_H$ ) of those analyzed exposures. Columns 3 & 4 give the values of the parameters from the *diskbb* model. Columns 5-8 give the values of the parameters from the *pexrav* model. Columns 9 & 10 give the values of the constants needed to achieve simultaneous broadband fitting. Column 11 gives the values of the  $\chi^2/DOF$  for each fitting.

Time	TBabs	diskbb		pexrav				Fitting constants		Fitting Stat
MJD	$N_H$	$T_{in}$ (keV)	Norm	$\Gamma$	$E_{cut}$	$rel_{frac}$	Norm	Constant1	Constant2	$\chi^2/DOF$
(1)	(2)	(3)	(4)	(5)	(6)	(7)	(8)	(9)	(10)	(11)
60373.9025	$5.74 \pm 0.21$	$1.61 \pm 9.4E - 2$	$97.67 \pm 2.40$	$2.58 \pm 7.6E - 3$	$82.09 \pm 3.14$	$0.32 \pm 8.2E - 2$	$22.92 \pm 2.42$	$1.07 \pm 1.2E - 2$	$1.07 \pm 1.7E - 2$	1554.44/1409
60374.9889	$5.77 \pm 0.25$	$1.39 \pm 1.0E - 2$	$197.9 \pm 4.76$	$2.61 \pm 1.1E - 2$	$81.96 \pm 1.37$	$1.3E - 2 \pm 1.8E - 4$	$30.02 \pm 2.60$	$0.98 \pm 1.7E - 2$	$0.98 \pm 2.4E - 2$	1451.32/1409
60375.9426	$5.59 \pm 0.28$	$1.49 \pm 1.2E - 2$	$130.5 \pm 3.13$	$2.62 \pm 1.0E - 2$	$76.35 \pm 1.02$	$5.0E - 2 \pm 1.6E - 4$	$28.55 \pm 2.60$	$1.04 \pm 1.6E - 2$	$1.08 \pm 2.8E - 2$	1397.76/1409
60376.9670	$5.08 \pm 0.37$	$1.32 \pm 6.0E - 3$	$477.5 \pm 8.52$	$2.64 \pm 1.7E - 2$	$44.79 \pm 2.48$	$0.10 \pm 9.9E - 4$	$22.20 \pm 2.60$	$1.09 \pm 2.9E - 2$	$1.17 \pm 5.0E - 2$	1522.15/1409
60377.9892	$5.91 \pm 0.38$	$1.28 \pm 4.4E - 3$	$404.0 \pm 8.48$	$2.83 \pm 1.4E - 2$	$42.62 \pm 2.82$	$5.0E - 2 \pm 8.9E - 4$	$35.61 \pm 2.44$	$1.07 \pm 1.9E - 2$	$1.10 \pm 7.6E - 2$	1400.06/1409
60378.8391	$6.21 \pm 0.30$	$1.45 \pm 4.6E - 3$	$165.8 \pm 5.25$	$2.96 \pm 1.1E - 2$	$106.4 \pm 3.81$	$5.0E - 2 \pm 7.0E - 4$	$46.95 \pm 2.41$	$1.04 \pm 1.4E - 2$	$1.15 \pm 4.3E - 2$	1620.60/1409
60379.8432	$5.84 \pm 0.24$	$1.53 \pm 5.8E - 3$	$73.88 \pm 3.82$	$2.86 \pm 9.9E - 3$	$179.2 \pm 1.95$	$0.14 \pm 6.0E - 3$	$35.99 \pm 2.43$	$1.03 \pm 1.5E - 2$	$1.17 \pm 3.5E - 2$	1474.45/1409
60380.9315	$5.62 \pm 0.11$	$1.42 \pm 3.8E - 2$	$100.3 \pm 3.03$	$2.81 \pm 5.4E - 3$	$124.1 \pm 2.04$	$5.0E - 2 \pm 2.7E - 4$	$30.59 \pm 2.80$	$1.04 \pm 1.6E - 2$	$1.00 \pm 3.6E - 2$	1409.79/1409
60381.7571	$6.00 \pm 0.11$	$1.39 \pm 3.7E - 2$	$120.4 \pm 2.69$	$2.67 \pm 7.8E - 3$	$15.94 \pm 0.53$	$5.0E - 2 \pm 2.3E - 4$	$35.90 \pm 2.76$	$1.04 \pm 1.5E - 2$	$1.33 \pm 6.6E - 2$	1632.36/1409
60382.9323	$6.30 \pm 0.21$	$2.09 \pm 2.0E - 2$	$16.39 \pm 1.28$	$2.90 \pm 2.4E - 2$	$53.09 \pm 1.82$	$5.0E - 2 \pm 7.7E - 4$	$42.62 \pm 2.75$	$0.99 \pm 1.2E - 2$	$1.13 \pm 5.9E - 2$	1431.01/1409
60383.8565	$5.35 \pm 0.29$	$1.80 \pm 2.4E - 2$	$30.82 \pm 1.21$	$2.69 \pm 1.0E - 2$	$44.00 \pm 1.23$	$0.15 \pm 1.1E - 3$	$25.27 \pm 2.77$	$1.01 \pm 1.5E - 2$	$1.48 \pm 5.1E - 2$	1433.76/1409
60383.9882	$5.66 \pm 0.21$	$1.63 \pm 2.0E - 2$	$35.96 \pm 2.24$	$2.86 \pm 8.1E - 3$	$210.6 \pm 2.40$	$5.1E - 2 \pm 1.6E - 3$	$29.15 \pm 2.83$	$1.04 \pm 1.6E - 2$	$1.03 \pm 4.1E - 2$	1440.43/1409
60384.1217	$5.52 \pm 0.17$	$1.58 \pm 2.0E - 2$	$41.10 \pm 2.30$	$2.87 \pm 6.6E - 3$	$373.0 \pm 5.13$	$0.11 \pm 1.0E - 2$	$27.24 \pm 2.83$	$1.05 \pm 1.4E - 2$	$1.02 \pm 3.5E - 2$	1321.88/1409
60386.5926	-	-	-	-	-	-	-	-	-	-

**Table 7.** Properties from spectral analysis using Model-3. Column 1 represents the MJD of those respective Exposure IDs for which we have performed spectral analysis. Column 2 gives the values of hydrogen column densities ( $N_H$ ) of those analyzed exposures. Columns 3 & 4 give the values of the parameters from the *diskbb* model. Columns 5-8 give the values of the parameters from the *pexriv* model. Columns 9 & 10 give the values of the constants needed to achieve simultaneous broadband fitting. Column 11 gives the values of the  $\chi^2/DOF$  for each fitting. For this model fitting, we have fixed the  $E_{cut}$  of this model to the  $E_{cut}$  of the *pexrav* model. Also, the disk temperature was set to  $10^6$  Kelvin. Since, the ionization parameter  $\xi$  has so small value, we did not estimate the error for this parameter.

Time	TBabs	diskbb		pexriv				Fitting constants		Fitting Stat
MJD	$N_H$	$T_{in}$ (keV)	Norm	$\Gamma$	$rel_{frac}$	$\xi$	Norm	Constant1	Constant2	$\chi^2/DOF$
(1)	(2)	(3)	(4)	(5)	(6)	(7)	(8)	(9)	(10)	(11)
60373.9025	$6.86 \pm 0.20$	$1.46 \pm 0.08$	$120.9 \pm 2.21$	$2.61 \pm 0.017$	$0.13 \pm 0.0761$	9.2E-09	$27.92 \pm 2.23$	$1.06 \pm 1.0E - 2$	$1.07 \pm 2.1E - 2$	1201.95/1409
60374.9889	$6.17 \pm 0.23$	$1.35 \pm 0.00$	$248.1 \pm 4.38$	$2.62 \pm 0.010$	$2.6E - 3 \pm 1.1E - 5$	4.4E-13	$30.06 \pm 2.39$	$1.00 \pm 1.2E - 2$	$1.00 \pm 2.7E - 2$	1210.39/1409
60375.9426	$5.50 \pm 0.26$	$1.50 \pm 0.01$	$135.5 \pm 2.89$	$2.63 \pm 0.010$	$9.6E - 2 \pm 0.0015$	1.6E-10	$27.59 \pm 2.39$	$1.05 \pm 1.3E - 2$	$1.10 \pm 3.1E - 2$	1230.26/1409
60376.9670	$5.03 \pm 0.34$	$1.33 \pm 0.00$	$447.3 \pm 7.85$	$2.65 \pm 0.015$	$0.10 \pm 0.0917$	1.0E-08	$22.47 \pm 2.39$	$1.07 \pm 1.8E - 2$	$1.16 \pm 4.6E - 2$	1279.92/1409
60377.9892	$5.92 \pm 0.35$	$1.29 \pm 0.00$	$389.1 \pm 7.82$	$2.82 \pm 0.013$	$6.1E - 3 \pm 8.2E - 5$	2.4E-13	$36.06 \pm 2.25$	$1.06 \pm 1.5E - 2$	$1.09 \pm 6.6E - 2$	1253.45/1409
60378.8391	$6.42 \pm 0.28$	$1.48 \pm 0.00$	$135.2 \pm 4.84$	$3.00 \pm 0.010$	$5.0E - 2 \pm 0.0065$	2.9E-09	$52.37 \pm 2.22$	$1.03 \pm 1.0E - 2$	$1.19 \pm 3.6E - 2$	1392.68/1409
60379.8432	$5.82 \pm 0.22$	$1.53 \pm 0.00$	$75.17 \pm 3.52$	$2.86 \pm 0.009$	$0.15 \pm 0.0555$	1.6E-10	$35.75 \pm 2.24$	$1.03 \pm 1.1E - 2$	$1.17 \pm 3.4E - 2$	1258.84/1409
60380.9315	$5.64 \pm 0.11$	$1.43 \pm 0.03$	$95.61 \pm 2.79$	$2.81 \pm 0.005$	$5.8E - 2 \pm 0.0256$	6.6E-09	$31.03 \pm 2.58$	$1.04 \pm 1.2E - 2$	$1.00 \pm 3.9E - 2$	1195.57/1409
60381.7571	$6.00 \pm 0.10$	$1.40 \pm 0.03$	$111.9 \pm 2.48$	$2.68 \pm 0.007$	$5.0E - 2 \pm 0.0022$	5.8E-12	$36.30 \pm 2.54$	$1.03 \pm 9.6E - 3$	$1.33 \pm 6.3E - 2$	1397.17/1409
60382.9323	$6.35 \pm 0.19$	$2.11 \pm 0.01$	$16.15 \pm 1.18$	$2.94 \pm 0.023$	$0.14 \pm 0.0012$	1.5E-09	$44.23 \pm 2.53$	$0.99 \pm 1.2E - 2$	$1.17 \pm 6.0E - 2$	1285.72/1409
60383.8565	$5.38 \pm 0.27$	$1.82 \pm 0.02$	$29.71 \pm 1.11$	$2.71 \pm 0.009$	$0.18 \pm 0.0010$	2.6E-09	$25.94 \pm 2.55$	$1.01 \pm 1.5E - 2$	$1.51 \pm 0.15$	1329.20/1409
60383.9882	$5.73 \pm 0.19$	$1.68 \pm 0.01$	$32.80 \pm 2.06$	$2.91 \pm 0.007$	$0.17 \pm 0.0152$	2.2E-11	$30.75 \pm 2.61$	$1.04 \pm 1.5E - 2$	$1.07 \pm 3.9E - 2$	1326.96/1409
60384.1217	$5.48 \pm 0.15$	$1.57 \pm 0.01$	$43.51 \pm 2.12$	$2.87 \pm 0.006$	$0.18 \pm 0.0092$	6.5E-11	$26.88 \pm 2.61$	$1.05 \pm 1.6E - 2$	$1.03 \pm 3.4E - 2$	1185.50/1409
60386.5926	$5.76 \pm 0.15$	$0.89 \pm 0.01$	$1437 \pm 10.9$	$3.37 \pm 0.138$	$2.24 \pm 0.1537$	3.8E-08	$18.45 \pm 1.27$	$1.00 \pm 2.0E - 2$	$1.64 \pm 0.14$	1277.63/1409

## APPENDIX

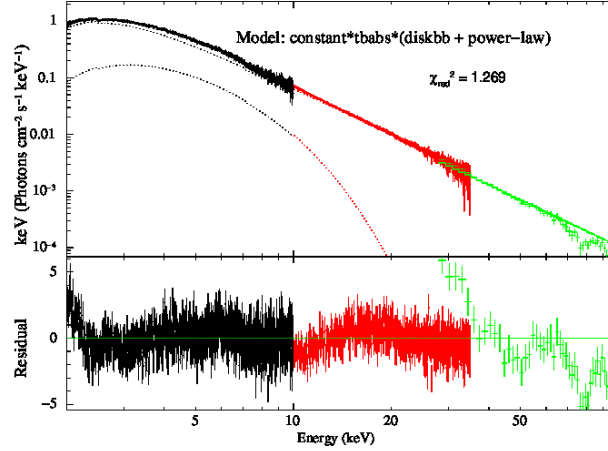


**Figure 15.** Model fitted unfolded spectrum for the combination of *tbabs*, *diskbb*, and *power-law* models. This is for the observation ID. P0614374001 (exposure ID: P061437400101-20240304-01-01).

Before fitting the data with the combination of phenomenological *broken power-law* or physical *pexrav* models with the combination of *diskbb* model, we tried to perform the spectral analysis using only the combination of *diskbb* and *power-law* models with the interstellar absorption model *tbabs*. The model combination reads as: *constant\*tbabs(diskbb + power-law)*. However, from Figure A.1, we notice that at the high energy end, after 20 keV, there is the presence of high residuals, which could be due to the presence of reflection radiation. Thus, we modeled the data using those above mentioned models to better fit the data, which we achieved.

As mentioned in the data analysis section, we also tried modelling using the relativistic reflection model *relxill*. However, we faced some problems while performing the spectral analysis. Although, for some exposures, the model fitted the spectra well, it was not the case for all the exposures. The best fit was achieved for the set of parameters, which were not in agreement with other models. We have found some degeneracy using the *relxill* model. Thus, we have not included this in our result in this draft.